THEORETICAL STUDY ON THIN FILM DYE SENSITIZED PHOTOVOLTAIC SOLAR CELLS

A Thesis
Submitted to the Graduate Faculty
of the
North Dakota State University
of Agriculture and Applied Science

By

Jiawei Gong

In Partial Fulfillment of the Requirements
for the Degree of

MASTER OF SCIENCE

Major Department:
Mechanical Engineering

December 2013

Fargo, North Dakota

North Dakota State University
Graduate School

Title

Theoretical Study on Thin Film Dye Sensitized Photovoltaic Solar Cells

By

Jiawei Gong

The Supervisory Committee certifies that this ***disquisition*** complies with North Dakota State University's regulations and meets the accepted standards for the degree of

MASTER OF SCIENCE

SUPERVISORY COMMITTEE:

Dr. Sumathy Krishnan
Chair

Dr. Xiangfa Wu

Dr. Long Jiang

Dr. G. Padmanabhan

Approved:

12/30/2013
Date

Dr. Alan Kallmeyer
Department Chair

ABSTRACT

This thesis presents two models of a dye-sensitized solar cell (DSC): diffusion model and electrical model. The main purpose is to investigate interfacial charge transfer and charge transport within the semiconductor/electrolyte layer under illuminated conditions. These two interrelated models confirm that diffusion is the major driving force for electron and ion transport, while the drift of electrons is negligible. The diffusion model was utilized to simulate the temperature influence on the overall efficiency of DSC with a consideration of the voltage loss at titanium dioxide (TiO_2)/ transparent conductive oxide (TCO) interface. It reveals that low temperature conditions have serious detrimental effects on the DSCs' performance. Further the electrical model was used to analyze the effect of diffusion/drift, dye loading, and electrode thickness on DSC performance. The predicted optimal electrode thickness ranges between $10 - 15\ \mu m$ which is consistent with the thickness ($10\ \mu m$) used in experimental studies published in the literature.

ACKNOWLEDGEMENTS

Foremost, I would like to thank my advisor Dr. Sumathy for her great help, support, patience and guidance during the development and completion of this thesis. I highly appreciated the great amount of freedom I was granted during my work and the dedicated support for this DSC simulation project. I highly appreciate my supervisory committee members Dr. Xiangfa Wu, Dr. Long Jiang, and Dr. Padmanabhan for their time and effort in guiding my work. In particular, I want to thank Dr. Xiangfa Wu for sharing his extensive knowledge on the device modelling, numerical methodology, and for enlightening discussions.

TABLE OF CONTENTS

LIST OF TABLES

LIST OF FIGURES

NOMENCLATURE

k_e	Electron relaxation rate constant
μ_e	Electron mobility
D_{I^-}	Iodide diffusion constant in nanotube
$D_{I_3^-}$	Triiodide diffusion constant in nanotube
C_{I^-}	Initial concentration of iodide (M)
$C_{I_3^-}$	Initial concentration of triiodide (M)
m_e^*	Effective mass of electron
ϵ	Effective relative dielectric constant
$E_{CB} - E_{Redox}^0$	Difference of conduction band and standard electrolyte redox energy (eV)
d	Thickness of inner cell (μm)
A	Cell area (cm^2)
p	Porosity of TiO_2 semiconductor
R_f	Roughness factor of TiO_2 semiconductor
T	Temperature (K)
k	Bolzmann constant, equal to 1.38066×10^{-23} JK^{-1}
Φ_0	incident photo flux (cm^{-2} s^{-1})
μ	electrical mobility
η	quantum yield of photogenerated electron/photoelectric conversion efficiency

Subscripts, Superscripts and Miscellaneous

oc	open circuit
sc	short circuit
[]	denotes concentration (M)
0	denotes concentration

1. INTRODUCTION

1.1. General

Nobel laureate Richard Smalley listed energy and environment problems on the top of challenges that we will face in next 50 years. The increase in energy consumption has accelerated the depletion of the earth's oil reserves, and the combustion exhaust of fossil fuels has resulted in the environmental contamination and greenhouse effect. Currently, worldwide concerns of such problems significantly spur the technological endeavor of renewable and green energy. The European Union (EU) has set a goal that by 2020 renewable energy should account for 20% of the EU's final energy consumption (10.3% in 2008) [1]. In accordance, the American Recovery and Reinvestment Act in the United States has budgeted more than $80 billion in clean energy development aiming to reduce greenhouse gas emission by 28% by 2020 [2]. At present, a clear trend has been clear observed as the renewable energy share of global energy consumption in 2008 is 19%, which is a 50% increase compared to the 13% in 2003 [3,4].

Among all the renewable energy forms, solar energy has showed its advantages and potential for power generation. Solar radiation amounts to 3.8 million EJ/year, which is approximately 10,000 times more than current energy needs [5]. From the perspective of energy conservation and environmental protection, it is desirable to directly convert solar radiation into electrical power by the application of photovoltaic devices. It is shown in Figure 1, in the 5-year period between the end-2004 to 2009, solar photovoltaic energy generation has increased at 60% annual growth rate, fastest among all other the renewable technologies [4].

High cost and complicated production process exclude traditional silicon-based solar cells from the domestic and other commercial applications. However, in recent decades several organic solar cells have been invented that combine the lightweight and flexibility of organic molecules

with the low module cost [6,7]. In terms of efficiency and easy fabrication, the dye-sensitized solar cell is one of the most promising alternatives to the silicon solar cells.

In 1991, Oregan and Grätzel built the first dye sensitized nanocrystalline solar cells whose photoelectric energy conversion rate reached 7.1% and incident photon to electrical current conversion efficiency was approximately 80% [8]. This simple structure and low cost technology of their study have further stimulated great research interest to improve the efficiency of dye-sensitized solar cells which has attained ca. 10% [9], a level deemed as necessary for commercial use [10].

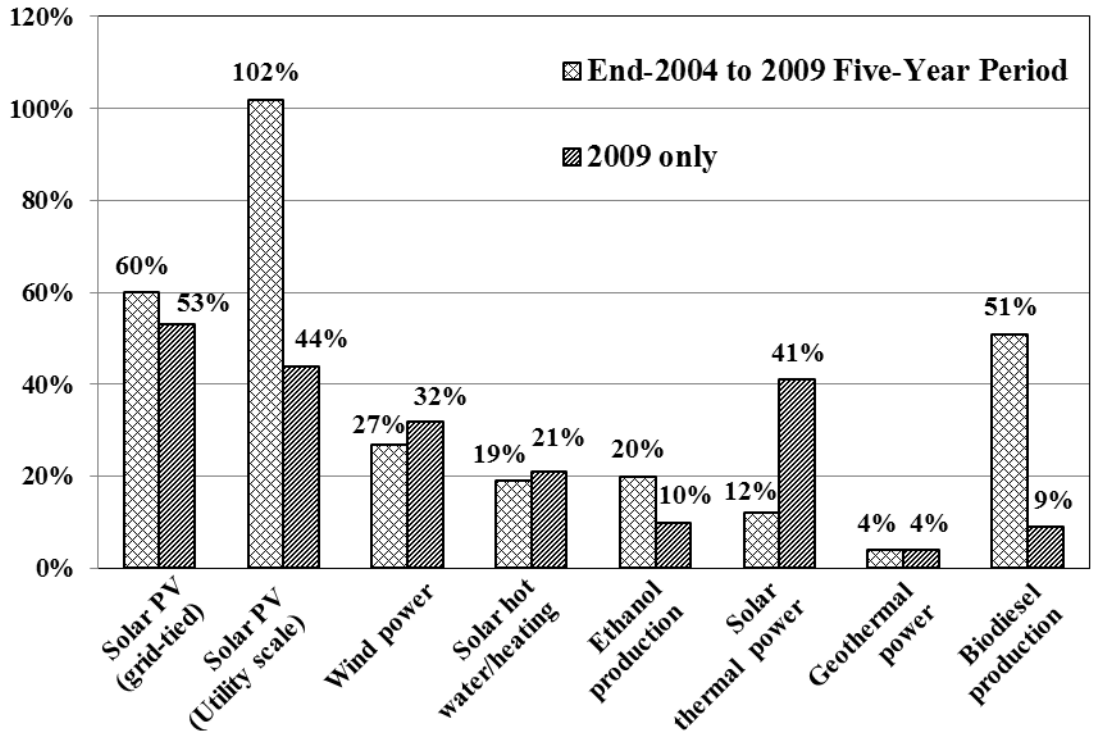

Figure 1. Average annual growth rates of renewable energy capacity, the end-2004 to 2009 [4].

1.2. System Description

Dye-sensitized solar cell (DSC) is a semiconductor photovoltaic device that directly converts solar radiation into electric current. The operational principle of DSC is illustrated in the Figure 2. The system consists of the following:

(i) a transparent anode make up of a glass sheet treated with a transparent conductive oxide layer;

(ii) a mesoporous oxide layer (typically, TiO_2) deposited on the anode to activate electronic conduction;

(iii) a monolayer charge transfer dye covalently bonded to the surface of the mesoporous oxide layer to enhance light absorption;

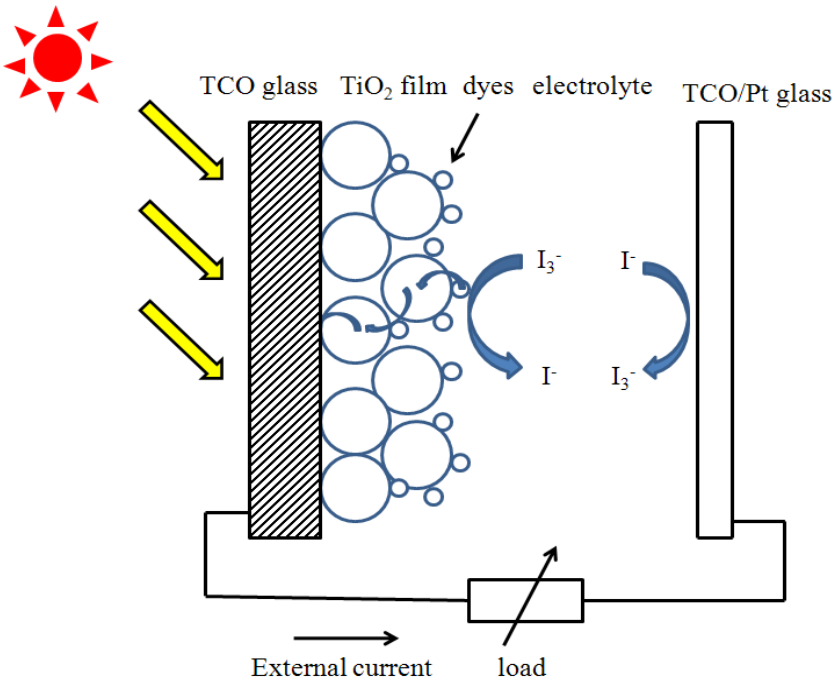

Figure 2. Schematic of operation of the dye-sensitized solar cell.

(iv) an electrolyte containing redox mediator in an organic solvent effecting dye-regenerating; and

(v) a cathode made of a glass sheet coated with a catalyst (typically, platinum) to facilitate electron collection.

When exposed to sunlight, the dye sensitizer gets excited from which an electron is injected into the conduction band of the mesoporous oxide film. These generated electrons diffuse to the anode and are utilized at the external load before being collected by the electrolyte at cathode surface to complete the cycle.

In order to enhance electrical conductivity and light transmittance, conducting glass is used as the substrate. There are mainly two types of conducting glass: indium-doped tin oxide (ITO) and fluorine-doped tin oxide (FTO). The standard to select a proper type is sometimes ambiguous because of the variety of cell configurations and materials [11]. The semiconductor electrode is usually a layer of nanocrystalline titanium dioxide (TiO_2), a thin film deposited on the conducting glass film with the thickness ca. 5-30 μm, which plays an important role in both the exciton dissertation and the electron transfer process. The porosity and morphology of the TiO_2 layer are dominant factors that determine the amount of dye molecules absorbed on its surface which can provide an enormous area of reaction sites for the monolayer dye molecules to harvest incident light. A large number of artificial dye molecules have been synthesized since the first introduction of dye-sensitized solar cells and some of them have already been successfully commercialized such as N3, N719 and Z907. Desirable dye molecules have to meet certain requirements, such as match with the solar spectrum, long-term operational stability, and firm graft on the semiconductor surface. In addition, their redox potential should be high enough to facilitate the regeneration reaction with a redox mediator [12]. As such, Iodide and triiodide (I^-/I_3^-) redox couple is the most commonly used in a liquid electrolyte, while other solid-state and quasi-solid state electrolytes like organic hole-transport material and polymer gel are also applicable [13-17]. Platinum is generally used as the cathode to catalyze the reduction of the oxidized charge mediator [18].

1.3. Outline of Thesis

This thesis is presented in six chapters. Chapter 2 provides detailed information on the DSC operation, and presents a literature review of experimental and theoretical studies of DSCs. It discusses important results from the literature that provide a basis of knowledge for work presented in the subsequent chapter. It also provides a review of the mathematical modeling of DSCs to date. Additionally, modeling background and electrochemical results used in the development of the model equations are presented. Chapter 3 provides an outline of the study's objectives.

In Chapter 4, initially a simple theoretical model integrating a thermionic emission model into a diffusion model is derived. Then a one-dimensional electrical model with simplified boundary conditions is developed. Diffusion and migration are modeled within semiconductor porous structure and within the electrolyte filled pores. Transport phenomenon is modeled based on the diffusion of charged species as a result of concentration gradients, as well as migration due to electric fields in the electrolyte and semiconductor. The numerical approach applied to obtain results is also discussed.

In Chapter 5, the effects of operating temperature and Schottky barrier height on DSC's performance are investigated to evaluate the device performance under extreme weather conditions. Then numerical results for a standard DSC setup are compared with experimental data. The role of electrical field in charge transport is examined. The effects of various design and operating parameters on the power output and efficiency of the solar cell are also investigated. Simulation results include: the model validation, the outcomes and implications of parametric study, and a comparison to existing models.

Finally, in chapter 6 the results and conclusions of the modeling work presented in this thesis are summaries. A discussion suggesting further directions for the modeling work and numerical investigations is presented.

Appendix A illustrates the procedure of a typical relaxation method, and Appendix B contains a listing of the numerical code developed to solve the proposed electrical model.

2. LITERATURE REVIEW

2.1. Panchromatic Sensitizers

The striking feature of dye-sensitized solar cell is the mechanism by which energy is absorbed from photons. In these cells, photons are absorbed by dye molecules then transported to the current collector via TiO_2 particles. This is in contrast to traditional pn-junction solar cells where photons are absorbed by the semiconductor itself exciting electrons in the valence band to enable promotion into the conduction band. Therefore, the ideal dye molecule has to meet several requirements that guide effective molecular engineering: i) sensitizer should be able to absorb all incident light below the near-IR wavelength of approximately 920 nm; ii) it must carry carboxylate or phosphonate group to anchor on the surface of semiconductor oxide; iii) the lowest unoccupied molecular orbital (LUMO) of sensitizer must match to the edge of the conduction band of the oxide to minimize the energetic potential losses during the electron transfer reaction; iv) the highest occupied orbital (HOMO) of the sensitizer must be sufficiently low to accept electron donation from an electrolyte or a hole conductor material; v) it should be stable enough to endure 10^8 turnovers corresponding to 20 years exposure to sunlight without apparent degradation.

Since its discovery in 1993 [19], cis-RuL_2-$(NCS)_2$ (N3 dye) has become the paradigm of the efficient charge-transfer sensitizer for nanocrystalline TiO_2 films. It has an absorption threshold around 800 nm covering the visible to the near-infrared region of solar spectrum. In addition, in N3 dye can the photoexcited electrons inject into the semiconductor layer efficiently via carboxylate groups which on the one hand firmly attach to the surface of TiO_2 as an electron transfer channel, and on the other hand link to the bipyridyl moiety to lower the energy of the ligand π^* orbital. Since the molecular electronic transition is a metal-to-ligand charge transfer, this structure is energetically favored in the electron injection process.

The performance of N3 dyes as a sensitizer is almost unmatched until the emergence of black dye. Nazeeruddin et al. [20] first reported the synthesis of a class of black dye which displays the panchromatic sensitization character over the whole visible range extending from the near-IR region up to 920 nm. Later conversion efficiency utilizing black dye was certified to be 10.4% by the Swiss Federal Institute of Technology in Lausanne (EPFL) [21]. Recently, by using black dye N749, Chiba et al. [22] could achieve the highest recorded overall efficiency of approximately 11.1% with an area of 0.219 cm^2 under standard AM 1.5 illumination. Until now, the photovoltaic performance of black dyes is expected to be superior to all other known charge-transfer sanitizers in terms of the whole range light absorption [23]. The ultrafast injection rate associated with the N3 dye is reported as less than 100 fs. The high incident-photon-to-current efficiency IPCE for the sensitized dyed films, in comparison to the IPCE for undyed TiO_2 film, are attributed to this efficient charge separation achieved by fast electron injection and a slow back electron transfer. Incident photon to current conversion efficiency comparison between N3 and N749 is presented in Figure 3. It is observed that the spectrum response of black dye extends ca. 100 nm wavelength to 900 nm the infrared region than that of N3 dye, which covers more near-IR region of the sunlight spectrum leading to a high IPCE value.

Though ruthenium (II) based dyes have provided a relatively high efficiency, there are several drawbacks of them: the high cost and the limited amount of noble metals, and also the sophisticated synthesis and purification steps. To address these issues, metal-free organic dyes have been prepared and applied in DSCs to replace Ru (II) based dyes [24].

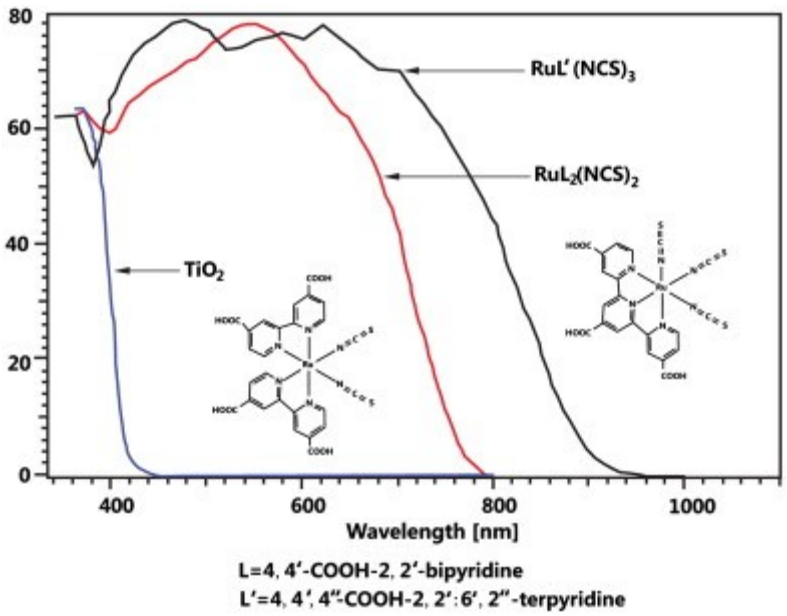

Figure 3. Incident photo to current conversion efficiency (IPCE) presents as a function of the wavelength for the standard ruthenium sensitizer N3 (red line), the black dye N749 (black curve), and the nanocrystalline TiO_2 film (blue curve). The chemical structures of the sensitizers are shown as insets [23].

At present, an overall solar-to-energy conversion efficiency 9.1% has been obtained by Hwang et al. [25] based on an organic metal-free dye TA-St-CA shown in Figure 4. It contains a p-conjugated oligo-phenylenevinylene unit with an electron donor–acceptor moiety for intramolecular charge transfer and a carboxyl group as an anchoring unit for the attachment onto TiO_2 nanoparticles. This configuration can be generalized as the donor-π bridge-acceptor structure shown in Figure 5, which implies an essential design principle for metal-free dyes. Guided by this design principle, Yella et al. [26] synthesized a donor-π bridge-acceptor zinc porphyrin dye (YD2-o-C8) which suppresses the interfacial electron back transfer from the nanocystalline TiO_2 film to the oxidized cobalt mediator, and leads to a strikingly high power conversion efficiency of 12.3% under simulated air mass 1.5 global sunlight.

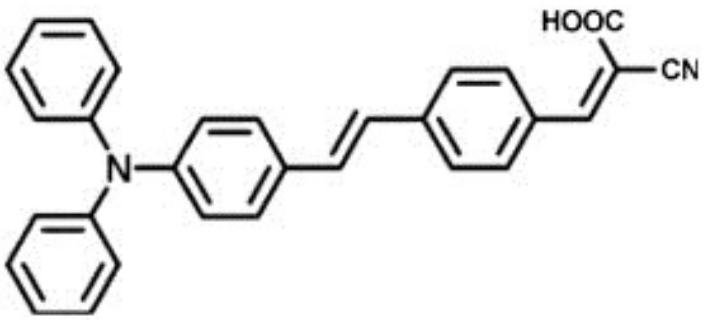

Figure 4. Molecular structure of TA-St-CA dye [25].

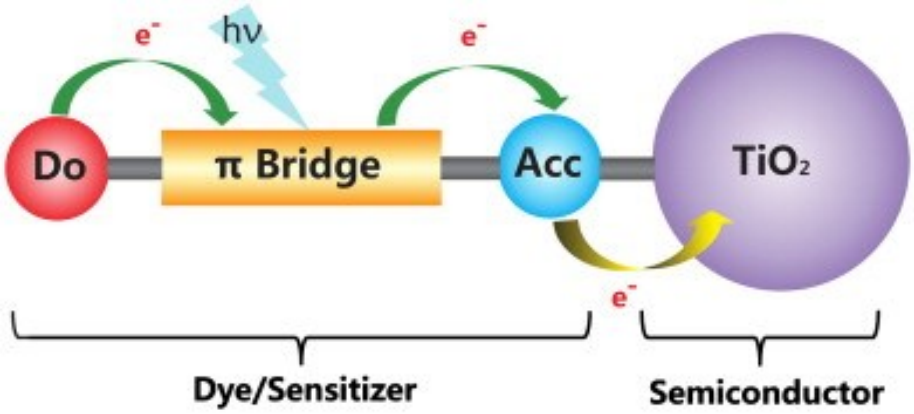

Figure 5. Design structure of metal-free organic dyes [24].

Another possible route to produce cost-effective dyes on a large scale is to extract natural dyes from plant sources. Natural dyes have many advantageous features such as their cost-efficiency, non-toxicity, and complete biodegradetion [27]. Although currently a device incorporating natural dyes has a much lower efficiency than those using synthesized dyes, it is noticeable that via structural modification, the natural dyes can have a performance as good as, if not better than their synthesized counterparts [28]. Thus, the structural optimization of natural dyes is a promising way to improve device efficiency.

2.2. Semiconductor Photoanode

Titanium dioxide (TiO_2) exits in three natural forms namely rutile, anatase and brookite. Among them the most stable form is rutile, which is at the equilibrium phase for any temperature. Though rutile form is more stable, anatase is perceived to be more chemically active when used in dye-sensitized solar cells. Anatase is metastable and has a trend to convert to rutile upon heating. Hence, the phase constituents are greatly influenced by the synthesis processing method. Nowadays, the commercial product DeGussa P25 has 80% anatase and 20% rutile at about 25 nm. In order to study this phase conversion influence, experiments were conducted to compare dye-sensitized rutile- and anatase-based TiO_2 solar cells [29]. Dye-sensitized solar cells (DSCs) fabricated with rutile and anatase films at the same thickness were subjected to the simulated AM 1.5 solar illumination. Results show essentially the same value of open-circuit voltage (V_{oc}), whereas the short-circuit photocurrent (I_{sc}) of the anatase-based cell is 30% higher than that of rutile-based cell. The difference in short-circuit current is attributed to the lower amount of dye absorption by the rutile film, owing to a relatively smaller specific surface area. The electron transfer rate in rutile film is generally slow in nature due to the low coordination number associated with the particle packing density, which is identified by intensity-modulated photocurrent spectroscopy.

Figure 6 shows that various semiconductor oxides have similar energy band structure as that of TiO_2. The structure similarity makes them not only a possible substitute to TiO_2 in DSCs, but also brings their own unique characteristic towards it. Intensive research has been dedicated to investigate this issue and potential application in other regimes. Zinc oxide (ZnO) is a promising alternative to TiO_2 because of the similar band structure and relatively high electron mobility ($1 - 5 \times cm^2V^{-1}s^{-1}$) [30]. Redmond et al. [31] reported the first transparent nanocrystalline ZnO films

prepared on a conducting glass substrate by sol–gel techniques. They are sensitized by cis-RuL_2-$(NCS)_2$ (N3 dye) and incorporated as the light-harvesting unit in a regenerative photoelectronchemical cell. The resulting device has a monochromatic IPCE of 13% at 520 nm and a simulated AM 1.5 solar conversion efficiency of 0.4%. This low efficiency is mainly due to the dissolution of the ZnO surface and formation of Zn^{2+}/dye aggregates in the acidic N3 solution. Later on, such obstacles are overcome by adding a base (KOH) to the acidic loading solution [32] or immersing the ZnO film in ethanolic solution under reflux [33]. Currently, Saito and Fujihara [34] fabricated ZnO photoanodes by a squeegee method and obtained the highest overall light-to-electric conversion efficiency of 6.58% under AM 1.5 with a large short-circuit photocurrent density of 18.11 mA cm^{-2}.

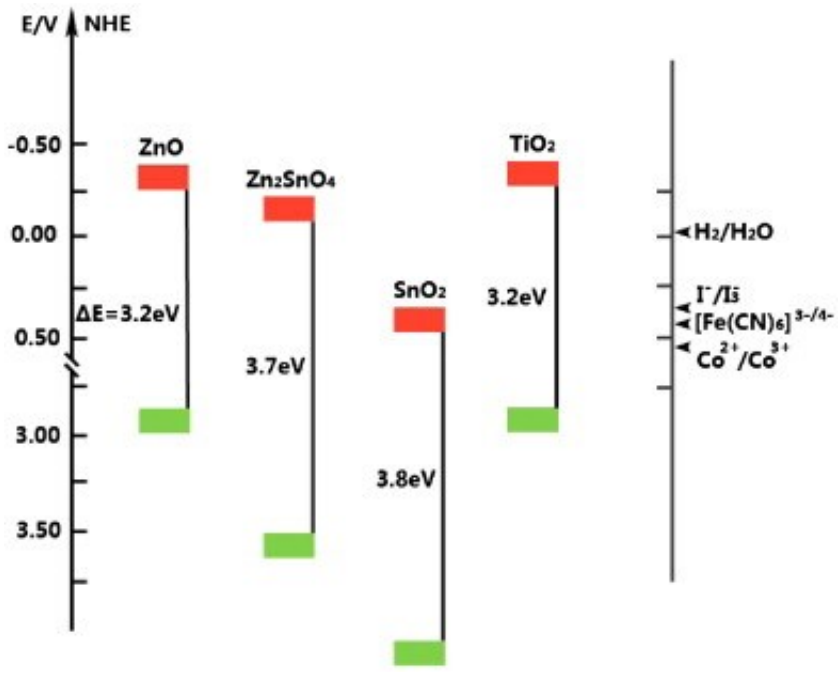

Figure 6. Band positions of several semiconductors and potentials of redox couples are represented using normal hydrogen electrode as reference.

Tin dioxide (SnO_2) is another attractive option having two main advantages over TiO_2: high mobility, and large band gap. At room temperature 300 K, SnO_2 electron mobility (ca. $100 - 200\ cm^2V^{-1}S^{-1}$ [35]) was measured by Fonstad and Rediker [36] which is three orders higher than that of TiO_2 (ca. $0.1 - 1\ cm^2V^{-1}S^{-1}$ [37]). The larger band gap of SnO_2 (3.8 eV), compared to TiO_2 (3.2 eV), would create fewer oxidative holes in the valence band under ultraviolet illumination, thereby reducing the dye degradation rate and improving the long time stability of DSCs. More positive band edge position facilitates electron injection from photoexcited dye molecules [38]. However, surprisingly the performance of dye-sensitized solar cells based on SnO_2 is so far much less than that based on TiO_2 [39]. The inferior photovoltaic properties of SnO_2 are ascribed to the faster electron recombination dynamics resulting from a 100-fold higher electron diffusion constant at matched electron densities, and from a 300 mV positive shift of the SnO_2 conduction band [40]. In addition, the lower isoelectric point (IEP) of SnO_2 (pH 4-5), compared with TiO_2 (pH 6-7), inhibit the adsorption of dye molecules with acidic carboxyl groups [41].

To overcome the above issues, conformal isolating oxide layers such as TiO_2, ZnO, MgO, and Al_2O_3 are coated on the surface of SnO_2 photoanode to suppress the back reaction, which can significantly improve the photoconversion efficiency. As reported by Senevirathna [42], the maximum overall light-to-electrical efficiency of about 7% can be achieved by MgO-coated SnO_2 DSCs.

Tan et al. [43] first synthesized large band gap energy (3.6 eV) ternary oxides Zn_2SnO_4 nanoparticles with desirable particle size from a hydrothermal process and tested it in the DSCs. It could achieve an overall light-to-electrical conversion efficiency of about 3.8% under AM 1.5 illumination. This efficiency is comparable to that of the single component ZnO solar cell (4.1%)

[44], and such Zn_2SnO_4 is more stable than ZnO against acidic dyes. Currently, the short electron diffusion length remains a limiting factor for the performance of Zn_2SnO_4 cells. These results are further confirmed by Huang et al. [44] who used Zn_2SnO_4 as electrode materials for the metal-free indoline DSCs.

Though prone to the low electron transfer and enhanced charge recombination, nanocrystalline TiO_2 has been regarded as the paragon of semiconductors since 1991. Up to now, no other material could replace its leading role in either research or commercial applications.

Electrons in the nanostructured TiO_2 film are charge compensated by ions in the electrolyte solution. Movement of electrons is therefore affected by the electrolyte. When the concentration of the electrolyte is decreased, electron movement is slower; conversely, when electrolyte concentration is much higher than electron concentration then the diffusion coefficient of electrons is closer to the apparent diffusion coefficient of electrons in nanostructured TiO_2. Studies on the DSC electrode morphology showed that the important light absorption coefficient α and electron transport coefficient D varied with porosity ***P*.**

2.2.1. Constant Overlap Method

It is assumed that all the TiO_2 nanoparticles are of the same spherical shape and a size with 10 nm radius. The physical overlap between two particles is illustrated in Figure 7. The following relationship among the geometric parameters can be derived [45]:

$$X = \left[\frac{4rY^2(3r - Y)}{3}\right]^{\frac{1}{4}} \tag{2.1}$$

$$S_1 = 2\pi r(h + Y) = 2\pi r\left[\frac{X^2(r - Y)}{4r^2 + X^2} + Y\right] \tag{2.2}$$

$$S_2 = 2\pi X a\theta = \frac{2\pi X^3}{4r}\arcsin\left[\frac{4r(r-Y)}{4r^2+X^2}\right] \tag{2.3}$$

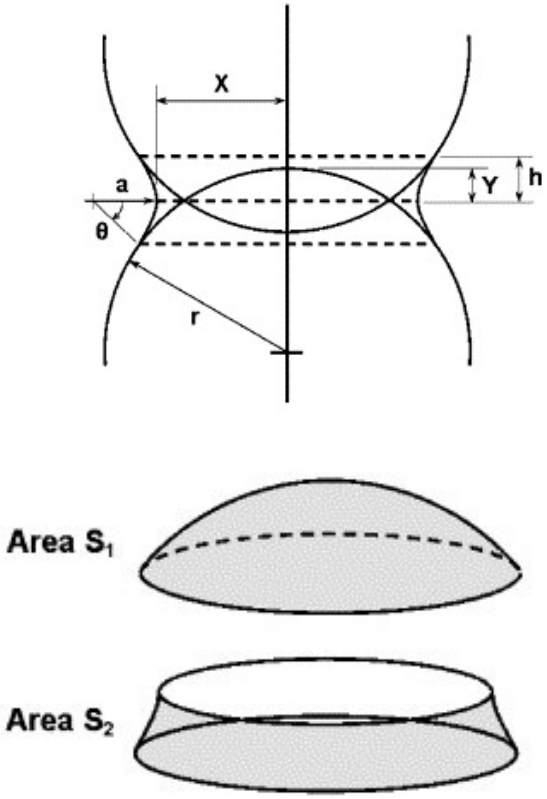

Figure 7. Illustration of neck formation of an overlap between two nanoparticles [45].

In the above equations, r is the radius of the particle; X is the radiusof the neck surface; Y is the overlap; and S_1 and S_2 are, respectively, the original and new surface areas of the deformed overlapping zone of one particle. The difference ΔS between S_1 and S_2 dictates the reduction in surface area due to one overlapping particle.

It is commonly observed that in an electrode of high porosity, one overlap causes about 2.5% reduction in the internal surface area, equivalent to a ΔS of 31 nm^2. Solving Eqs. (2.1)- (2.3) yields $Y = 0.39\ nm$. Therefore, it is assumed that at high porosity, overlap Y is equal to constant

$0.39\ nm$. The total number of particles N and the coordination number CN are related to P. As CN increases, P decreases. For densely packed particles with a maximum CN = 6, the porosity P is found to be 0.41. This P value serves as the transitional point as well as the lower bound ($P \geq 0.41$) for the use of this constant overlap method.

The relationship between α and P can be derived based on the total internal surface area of the dye-sensitized TiO_2 porous thin film. A series of equations are solved symbolically to obtain the α-P relationship:

1. total internal dye-sensitized surface area S

$$S = N(4\pi r^2 - CN\Delta S) \tag{2.4}$$

2. P defined as the ratio of the volume not occupied by TiO_2 to the total volume Vol

$$P = \frac{Vol - N\left(\frac{4}{3}\right)\pi r^3}{Vol} \tag{2.5}$$

3. Linear relationship between CN and P reported

$$CN = -10.29P + 10.22 \tag{2.6}$$

As α is directly proportional to S,

$$\alpha \propto (1 - P)(P + 2.89) \tag{2.7}$$

With a reference light absorption coefficient $\alpha = 5 \times 10^3 cm^{-1}$ for $P = 0.41$, the unknown factor can be determined and Eq. (2.7) becomes

$$\alpha = 2568(1 - P)(P + 2.89) \tag{2.8}$$

Based on both modeling and experimental results, effect of P on the diffusion coefficient D can be expressed as [46]:

$$D = \alpha|P - P_c|^{\mu} \tag{2.9}$$

where the constant a and μ, and the critical porosity P_c are $4 \times 10^{-4} cm^2 s^{-1}$, 0.82 and 0.76, respectively. It is shown that as the porosity increases, the distribution of the coordination numbers of the particles shifts from an emphasis on high coordination numbers to low ones, causing the electron transport pathway to become more tortuous and electron transport to slow. Another consequence of increasing the porosity is that the fraction of terminating particles (dead ends) in the TiO_2 film increases markedly, from less than 1% for a 50% porous film to 31% for a 75% porous film. It is estimated that during their respective transit through 50% and 75% porous in 10-μm thick films, the average number of particles visited by electrons increases by 10-fold, from 10^6 to 10^7.

2.2.2. Variable Overlap Method

Further reduction in P below the lower bound of the constant overlap method, i.e. $P < 0.41$, the overlaps rise above $0.39\ nm$. The internal surface area S is directly proportional to the square of P:

$$S \propto P^2 \tag{2.10}$$

As the light absorption coefficient α is assumed to be directly proportional to S,

$$\alpha \propto P^2 \tag{2.11}$$

Using a reference $\alpha = 5 \times 10^3 cm^{-1}$ when $P = 0.41$. Eq. (2.11) can be deduced to

$$\alpha = 2.97 \times 10^4 P^2 \tag{2.12}$$

At low porosity, D also varies significantly with P

$$D = 1.69 \times 10^{-4}(-17.48P^3 + 7.39P^2 - 2.89P + 2.15) \tag{2.13}$$

2.3. Morphology Influence

2.3.1. Mesoporous Films

Mesoporous materials have pores between 2 and 50 nm in diameter. They usually have a continuous network that can either be ordered or disordered resulting in high internal surface area. Such a structure is favorable in heterogeneous chemical reactions because it provides a sufficient surface as reaction sites and facilitates mass diffusion by internal channels. The first dye-sensitized solar cells (DSCs) [8] based on the mesoporous TiO_2 films achieved a remarkable breakthrough. Until recently, the mosoporous film is still regarded as the most favorable electrode structure and widely used as a standard to study DSCs. Unique characteristics are found in mesoporous TiO_2 compared with its compact analogs: the low inherent film conductivity, no built-in electrical field within nanocrystalline particles, and three dimensional semiconductor/electrolyte interface contact [47]. Mesoporous film, though it yields extremely high specific surface area for dye uptake, could enhance the charge recombination to triiodine ions on the TiO_2/electrolyte interface. Thus, it is advantageous to have thinner films.

The mesoporous structure of the film depends on the preparation method, and its pore size distribution can be adjusted, for example, by controlling molar ratio of stearic acid to titanium etraisopropoxide as precursor [48]. Barbé et al. studied the microstructure of the mesoporous film correlation with preparation conditions such as precursor chemistry, temperature for hydrothermal growth, binder addition, and sintering conditions influence [49]. The film morphology and network geometry have a great influence on the electron transport dynamics of DSCs. The correlation between film morphology and photoelectrochemical performance of DSCs was investigated by Saito et al. [50]. It is reported that the amount of dyes adsorbed and photocurrent generated under illumination were proportional to the roughness factor (R_f) under 1400, and the

diffusion limit of electrolyte rarely affected the photocurrent under 1 sun irradiance. Benkstein et al. [46] found the electron diffusion coefficient D has a power-law dependence on the film: $D \propto |P - P_c|^{\mu}$, where the critical P_c is 0.76 ± 0.01 and the conductivity exponent μ is 0.76 ± 0.05. It is shown that an increase in porosity shifts the distribution of corordination numbers of the particles to a low value, indicating a tortuous transport pathway and increased dead ends in the TiO_2 film.

Recently, a novel TiO_2 mesoporous network with multilayer structure was designed by Wang et al. [51]. In their work, multilayer films with different sized particles (diameter from ca. 100 nm to 23 nm) were fabricated and aligned layer by layer on the conducting glass to enhance light scattering. This structure effectively increased the IPCE at the red region and led to high cell efficiency 10.2%.

2.3.2. High Order Nanostructure

As mentioned in section 2.3.2, the conductivity of mesoporous film is much lower than its bulk analog. The electron diffusion coefficient determined by laser flash-induced transient photocurrent measurement [52] and intensity modulated photocurrent spectroscopy [53] is more than two orders of magnitude smaller than the value for bulk anatase crystal [54]. This puzzling phenomenon is due to the network defects which results in trapping/detrapping of electrons within grain boundaries, and can be predicted using the "Multiple trapping" model [55]. Therefore, replacing TiO_2 nanoparticles with highly ordered nanostructure is expected to achieve a rapid electron transfer by minimizing the crystal trapping sites. Recently, it has been shown that the DSCs based on the ordered arrays of TiO_2 or other metal oxide like ZnO manifest efficient charge separation and electron transfer feature.

Adachi et al. [54] reported a network structure of single-crystal-like TiO_2 nanowires formed through surfactant-assisted processes at a low temperature (353 K). The direction of crystal growth was controlled by changing the adsorption of surfactant molecules on the TiO_2 surface. A single-crystalline anatase exposing mainly the {101} plane exhibits excellent ruthenium dye adsorption, four times higher as compared to commercial product P-25, thus leading to a high overall cell efficiency of 9.3%.

Law et al. [30] prepared zinc oxide (ZnO) nanowire arrays and first applied them to the DSCs in 2005. ZnO nanowire arrays were formed according to the solution (ethanol) based process in which they adopted a modified seeded growth process to have a yield of long wires [56]. In their study, a 10-15 nm thick film of ZnO quantum dots was deposited onto FTO substrates by dip-coating. Nanowires grew from these nuclei through the thermal decomposition of a zinc complex. It is found the use of polyethylenimine (PEI), a cationic polyelectrolyte, has a striking effect as it hindered the lateral growth to increase the wire length. In this array, wire length and diameter varied from 16 to 17 μm and 130 to 200 nm, respectively. The prepared ZnO nanowire films are excellent conductors. The individual nanowire extracted from the arrays has a resistivity ranging from 0.3 to 2.0 Ω cm, with an electron concentration of $1 - 5 \times 10^{18}\ cm^{-3}$ and mobility of $1 - 5\ cm^2 V^{-1} s^{-1}$. The electron diffusivity for single dry nanowire can be calculated from the Einstein relation:

$$D_n = \frac{k_B T \mu}{e} \tag{2.14}$$

where k_B is Boltzmann constant, T is absolute temperature, μ is electron mobility and e is elementary charge. This value is several hundred times larger than the highest reported diffusivity for TiO_2 ($\approx 10^{-7} - 10^{-4}\ cm^2\ s^{-1}$) and ZnO ($\approx 10^{-5} - 10^{-3}\ cm^2\ s^{-1}$) nanoparticle films, which confirms that direct electrical pathways formed by the nanowires ensure rapid collection of

carriers generated throughout the device. At a full Sun intensity of $100 \pm 3\ mW\ cm^{-2}$, the dye-sensitized solar cells with ZnO arrays were characterized by short-circuit density $J_{sc} = 5.3 - 5.85\ mA\ cm^{-2}$, $V_{oc} = 0.61 - 0.71\ V$, $FF = 0.36 - 0.38$, and overall conversion efficiency $\eta = 1.2 - 1.5\%$. The conversion efficiency is limited primarily by the surface area of the nanowire array, which only has one-fifth the active surface area of a nanoparticle anode.

Nanotubes with a hollow cavity structure offer a huge active surface area compared to that of nanowires. Attempts have been made to prepare such nanostructures. Adachi et al. [57] synthesized titania nanotubes by surfactant-assisted templating mechanism using molecular assemblies composed of surfactant molecules, *i.e.*, laurylamine hydrochloride, titanium alkoxide, and tetraisopropylorthotitanate modified with acetylacetone, as a template. These nanotubes have outer and inner diameters of about 10 and 5 nm, respectively, and a length ranging from 30 nm to several hundred nanometers. The thin-film electrode made of titania nanotubes collected more than two times larger short-circuit current density than that of P-25 in the thin-film region, which explains the higher light to electricity conversion efficiency ($\sim 5\%$).

Because insufficient active surface area is the limiting factor of nanotube application in DSCs, it is of key interest to understand its dependence on the geometry parameter. To this end, both theoretical and experimental studies have been conducted recently. Assuming an idealized nanotubular structure as Figure 8 (a), the purely geometric roughness (physical surface area of the film per unit of projected area) is expressed as [58, 59]:

$$R_f = 1 + \frac{4\pi L(D + W)}{\sqrt{3}(D + 2W)^2} \tag{2.15}$$

where D is inner diameter, W is wall thickness, and L is the tube length. From the plot Figure 8 (b), it is shown that larger surface area is easily obtained by nanotubes with small porosity. Although

each surface area of nanotubes is reduced according to the reduction in porosity, more nanotubes could be used to offset the individual loss to increase the total surface area (equivalent area).

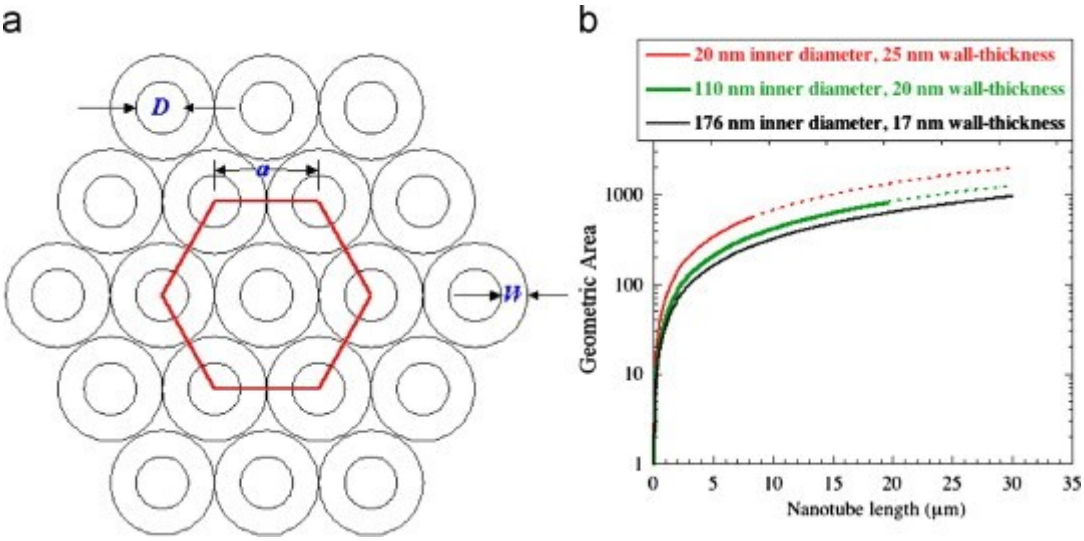

Figure 8. (a) Idealized unit cell of TiO_2 nanotube array with inner diameter D, wall thickness W, and $a = D + W$ and (b) geometric roughness factor Vs nanotube length [59].

Recently, Lei et al. [60] fabricated large-scale, noncurling anatase crystalline TiO_2 nanotube arrays on a FTO substrate via a four step process: (i) fabrication of TiO_2 nanotube on Ti foil by anodization, (ii) detachment of the amorphous free-standing TiO_2 nanotubes via ultrasonic treatment, (iii) transfer and adhesion to FTO substrates, and (iv) two-steps annealing treatment. For a 20.8 μm length array, an overall photoconversion efficiency of about 8.1% can be achieved.

2.3.3. Other Novel Morphology

Besides the nanowire and nanotube structure, many other highly ordered one-dimensional (1D) nanoarrays have been applied to dye-sensitized solar cells in recent years. A novel structure

of submicrometer-sized mesopores TiO_2 beads was first reported by Chen et al. [61]. In their work, highly crystallized mesoporous TiO_2 beads with surface areas of up to $108.0\ m^2\ g^{-1}$ and tunable pore sizes (from 14.0 to 22.6 nm) have been prepared through a combined sol-gel and solvothermal process. This structure promotes light scattering on the electrodes, without sacrificing the accessible surface for dyes. An overall light conversion efficiency of 7.2% has been achieved by using these mesoporous TiO_2 beads as an electrode.

Yang et al. [62] first synthesized ordered hollow TiO_2 hemisphere films for photoelectrodes in DSCs. They combined colloidal templates and rf-sputtering to deposit quasi-ordered hollow TiO_2 hemispheres onto conducting glass substrates with tunable hemisphere size and shell thickness. The hollow structure promotes electron transport and enhances dye loading by a large surface area. An enhanced photo-conversion efficiency of 3.49 % was achieved under air mass 1.5 illumination. Similar work has been conducted by Qian et al. [35]. They first synthesized TiO_2-coated multilayered SnO_2 hollow microspheres (MHSs, as shown in Figure 9) by two steps. First, SnO_2 MHSs were prepared by a chemically induced self-assembly reaction of aqueous sucrose/$SnCl_4$ solution under a hydrothermal condition. The second step was to coat TiO_2 nanocrystallites onto the SnO_2 MHSs by impregnating in and then hydrolyzing $TiCl_4$ to form a surface layer of TiO_2. It was found that TiO_2-coated multilayered hollow SnO_2 microspheres exhibited a high photoconversion efficiency of 5.65%, a 34% improvement compared to the TiO_2-nano-SnO_2 film.

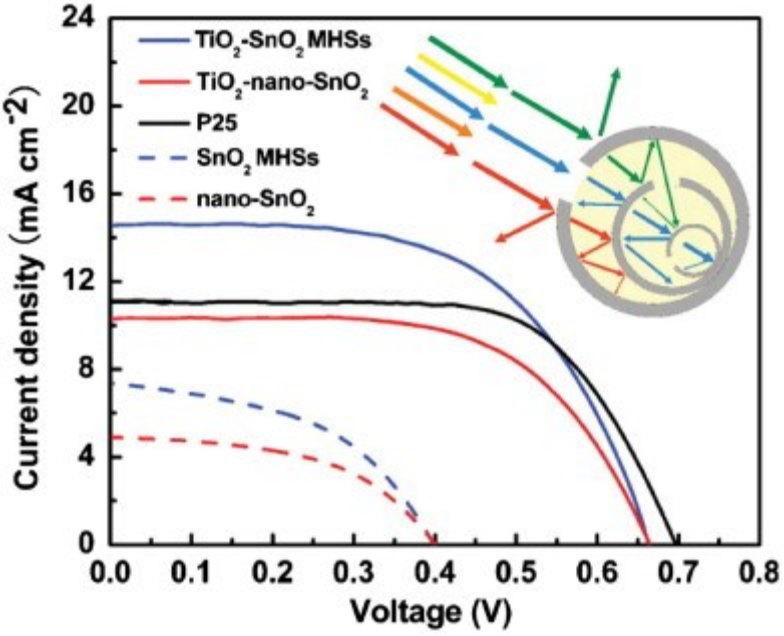

Figure 9. *j-V* characteristics of DSCs for different photoelectrode films [35] (The inset illustrates the multiple reflecting and scattering of light in the multilayered hollow spheres.).

2.4. Electrolyte Development

The electrolyte is a key component of all dye-sensitized solar cells (DSCs). It functions as charge carriers collecting electrons at the cathode and transporting the electrons back to the dye molecule. In terms of the cell efficiency, the most popularly used electrolyte is the iodide/triiodide (I^-/I_3^-) redox couple in an organic matrix, generally acetonitrile. However, there exist undesirable intrinsic properties which are inherent of a liquid electrolyte significantly affecting a device's long-term durability and operational stability. For example, not only the leakage of toxic organic solvent will cause environmental contamination, but also the evaporation of volatile iodine ions will increase the overall internal resistance by lowering concentration of the charge carrier. To overcome these disadvantages, research has been conducted to develop non-traditional electrolytes e.g. room temperature ionic liquids (RTILs), quasi-solid state and solid state electrolytes.

2.4.1. Liquid Electrolyte

The most commonly used liquid electrolyte, namely iodide/triiodide (I^-/I_3^-), works well mainly due to its kinetics as shown in Figure 10 [63]. The electron injection into the TiO_2 conduction band occurs in the femtosecond time range which is much faster than the electron recombination with I_3^-, and the oxidized dye preferably reacts with I^- than combining with the injected electrons. In the electrolyte, the I_3^- diffuses to cathode to harvest electrons and in turn produce I^- which diffuses in the opposite direction towards the TiO_2 electrode to regenerated dye molecules. The diffusion coefficient of I_3^- ions in the porous TiO_2 structure is about $7.6 \times 10^{-6}\ cm^2/s$ [64].

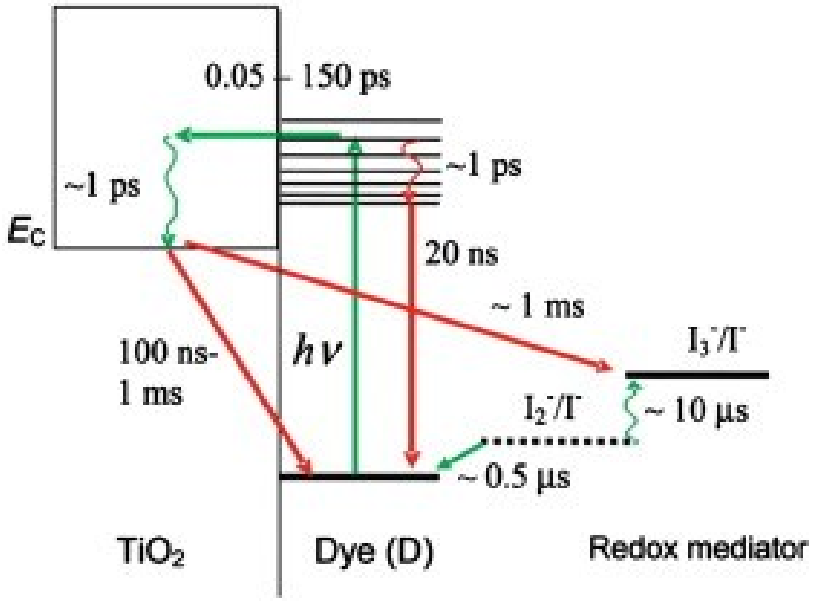

Figure 10. Kinetics of the cis-$Ru(dcbpy)_2(NCS)_2$-sensitized TiO_2 solar cell with I^-/I_3^- redox mediator [63].

One important issue to be considered when using the I^-/I_3^- redox couple is its concentration. At low iodine concentration, it is difficult to maintain sufficient electrolyte conductivity and rapid redox reaction. On the other hand, when iodine concentration is high, electron recombination at the TiO_2 interface deteriorates the performance of DSCs and meanwhile the rate of light absorption

by redox couple is increased [65]. The exact quantitative relationship is expressed in Eq. (5.1) which shows that electron recombination process determines the open circuit voltage (V_{oc}) which depends on the concentration of triiodide in the TiO_2.

It is found that recombination can be suppressed by introducing additives to the electrolyte such as 4-tert-butylpyridine (4TBP) [66], guanidium thiocyanate [67], and methylbenzimidazole (MBI) [68]. These additives can improve the efficiency and stability, though they do not participate in the fundamental photo-electrochemical processes. The most probable mechanism is that these additives when absorbed by the TiO_2 surface block the reduction sites to keep electron acceptor molecules away from contact. A similar phenomenon was observed by Zhang et al. [69] when adding co-adsorbents in a dye bath.

In theory, the maximum voltage generated in DSCs is determined by the difference between the quasi-Fermi level of the TiO_2 and the redox potential of the electrolyte, about 0.7 V under solar illumination conditions. In order to obtain a higher open circuit voltage and circumvent the corrosion of I^-/I_3^- redox couple, a variety of alternative redox couples have been introduced to DSCs such as Br^-/Br_3^-, $SCN^-/(SCN)_2$, $SeCN^-/(SeCN)_3^-$, and Co(II)/Co(III) complex. Recently, Wang et al. [70] reported a new disulfide/thiolate redox couple that has negligible absorption in the visible spectral range and achieved an unprecedented efficiency of 6.4% under standard illumination test conditions. This novel redox couple set a new benchmark for iodide-free DSCs by offering a viable pathway to scale up and practical applications. The best alternative redox couple to date is cobalt polypyridine redox reported by Feldt et al. [71]. They optimized organic dyes and cobalt polypyridine redox mediators for DSCs. By using a triphenylamine-based organic dye in combination with tris(2,2′-bipyridyl)cobalt(II/III), an overall conversion efficiency of about

6.7% was achieved recording an open-circuit potential of more than 0.9 V when exposed to AM 1.5 G illumination.

Other than redox couple electrolyte, a new type of liquid electrolyte, i.e. room temperature ionic liquids (RTILs), has shown promising potential to serve as an alternative electrolyte. RTILs are a group of organic salts containing cations such as imidazolium, pyridinium and anions from the halide or pseudo halid family [72]. Because of these structures, they function simultaneously as iodide source and as solvent [73]. It is expected that RTILs could solve the sealing problem and enhance the stability by virtue of their inherent characteristics like good chemical and thermal stability, negligible vapor pressure, non-flammability, and high ionic conductivity.

The first application of RTIL to DSCs was reported by Papageorgious et al. [74] in 1996. In their study methyl-hexyl-imidazolium iodide (MHImI) was added as an iodide resource which was found to be the least viscous iodide molten at room temperature and not sensitive to water moisture. Outstanding stability was achieved with an estimated sensitizer turnover in excess of 50 million times. However, the photovoltaic performance was very low due to low iodide concentration, as well as its viscosity being relatively high (1800 cP at 25 °C) compared to the water (0.890 cP). Research continues on the application of RTIL, and many other molten salts, such as 1,3-dialkylimidazolium, 1,2,3-trialkylimidazolium, and N-alkylpyridinium [75], have been tested with DSCs for their compatibility. The current milestone for ionic electrolyte development is that eutectic salts have been used to achieve a remarkable efficiency of 8.2% [76].

2.4.2. Solid-State Electrolyte

A solid-sate electrolyte is considered to be an alternative to the liquid electrolyte, because it could achieve a better mechanical stability and simplified fabrication processes. It is an essentially simple idea that replaces the liquid electrolyte with inorganic p-type semiconductors or organic hole transporting materials to eliminate the evaporation and leakage of liquid electrolyte. In this sense, the n-type semiconductor and p-type sensitizer make dye-sensitized solar cells inevitably analogous with traditional Si-based p–n junction solar cells in principle. A suitable hole-transport material must have a band gap structure compatible with the highest occupied molecular orbital (HOMO) level of the dye and the conduction band of TiO2 to drive the charge-transfer process. The main difficulty in realizing such a solid-state electrolyte device is to form an intimate contact at the p–n junction interfaces.

The first p-type semiconductors acting as hole-transport materials were CuSCN and CuI, introduced by Tennakone et al. [77] and O'Regan and Schwartz [78]. In their first step, they could achieve an overall efficiency less than 1%, due to the formation of unfilled voids in the TiO_2 intercrystallite. During the deposition process, p-CuI crystalline semiconductors experience a rapid crystal growth. The formation of a crystal with a dimension exceeding that of TiO_2 pores will interfere with the filling process, leaving a large portion of pores unfilled. Later Kumara et al. [79] found an effective crystal growth inhibitor triethylaminehydrothiocyannate (THT) to improve the cell efficiency to 3.75%. Recently, a novel working electrode TiO_2/CuI/Cu was reported by Heng et al. [80]. In their study, the CuI layer was deposited on a copper mesh to form a p–n junction with TiO_2. This structure forms a single directional pathway for efficient electron transport, which led to a high conversion efficiency of up to 4.73% under 1 sun illumination. As for p-type organic semiconductors, spiro-OMeTAD has proven to be the most successful one. It was initially

presented by Bach et al. [81] in 1998, and since then the conversion yield of its device has been increasing and has reached about 4%.

2.4.3. Quasi-Solid Electrolyte

As mentioned in the last two sections, most of the works have reported that the conversion efficiency of DSCs using solid electrolyte is lower, typically less than 5%. This is due to the fact of poor contact at TiO_2/electrolyte interface and conductivity of these materials is generally low [82]. In order to circumvent the above drawbacks, an alternative solution is proposed and attempted where both liquid and solid electrolytes can be combined to form a quasi-solid electrolyte, or gel electrolyte. Apparently, there are several advantages of using gel electrolyte: (i) relatively high ambient ionic conductivity ($6 - 8\ mS\ cm^{-1}$), (ii) intimate interfacial contact with TiO_2, and (iii) remarkable electrolyte stability. At the initial step, the solvent with a low viscosity penetrates the TiO_2 mesopores to form a good contact. After gelation volatile liquid solvent is encapsulated within a gel network that prevents the electrolyte evaporation and leakage.

Wang et al. [83] demonstrated that PVDF-HFP polymer can confine MPN-based liquid electrolyte into gel without hampering charge transport of the triiodide/iodide couple inside the polymer network. A conversion yield higher than 6% was obtained. In addition, the cell with such gel electrolyte sustained heating for 1000 h at 80 °C, maintaining 94% of its initial performance. Later, the ionic liquid was seminally solidified by adding silica nanoparticles to produce an ionic liquid-based quasi-solid state electrolyte which achieved an efficiency of 7% [84].

2.5. Transparent Conducting Substrate

Apart from semiconductor oxide film, the transparent conducting substrates also play an important role in dictating the DSCs' performance. They are thin layer films which function as a current collector and a support of the semiconductor layer in DSCs. They have two important features: the high optical transparency which allows natural sunlight to pass through to the beneath of the active material without unwanted absorption of the solar spectrum, and the low electrical resistivity which facilitates electron transfer process and reduces energy loss.

Indium tin oxide (ITO, In_2O_3:Sn) films exhibit an ideal transparency (transmittance over 80%) and resistivity (ca. $10^{-4}\ \Omega\ cm$) at room temperature, so they are widely used as transparent conducting oxide in the field of optoelectronic device. It is notable that depending on the preparation method, the electrical properties of ITO films disperse widely. As reported by Tahar[85], In_2O_3:Sn synthesized from $In_2(SO_4)_3$•nH_2O and $SnSO_4$ by dipping method has the resistivity of $6 - 8 \times 10^{-4}\ \Omega\ cm^{-1}$. The low resistivity is believed to be the result due to the large free carrier densities, which are caused by (i) substitution of indium atom by tin atom releasing one extra electron, and (ii) oxygen vacancies acting as two electron donors [86,87]. However, their low resistivity property could be deteriorated during the calcinations process in the DSCs fabrication.

Typical fabrication of the photoelectrodes in DSCs involves coating and sintering TiO_2 pasta on conducting substrates at high temperature ca. 450 °C to improve the electronic contact. When ITO film is exposed to high temperature above 300 °C, the sheet resistance increases drastically, leading to very low device efficiency. Such increased resistance can be explained by the reduced carrier density. When ITO films annealed at high temperature, oxygen in the atmosphere starts to fill the oxygen vacancies which function as an electron supplier. To prevent

the loss of charge carriers in high temperature, a double layer structure has been utilized to achieve the thermal stability of ITO-based substrates. The thin layer metal oxides, such as ATO (SnO_2:Sb antimony-doped tin oxide), AZO (aluminum-doped zinc oxide), and SnO_2, have been sputtered onto the ITO surface to form the double layer which has proved to be a much better structure than single layer ITO [88].

Apart from the listed transparent conducting oxides, fluoride-doped tin oxide (SnO_2:F, FTO) with a similar structure and working principle as ITO has been attempted. FTO-coated glass substrates have 70%-80% transmittance in the visible range at a thickness of 750 nm, approximately 10% less than that of ITO substrates. The sheet resistance of FTO coated glass is $< 12\,\Omega/sq$, about 20% lower than that of ITO coated glass ($15\,\Omega/\mathrm{sq}$). However, for the comparable transparency and conductivity, FTO-coated glass costs less than one third of ITO-coated glass [89].

Studies have been conducted to compare the performance of ITO and FTO based DSCs by Sima et al. [90]. They fabricated DSCs in a standard configuration and TiO_2/TCO/glass layers were subjected to thermal treatment at 450 °C for 2 h in an oxygen atmosphere. It was found that the sheet resistance value of ITO increased from the original $18\,\Omega/\mathrm{sq}$ to $52\,\Omega/\mathrm{sq}$ after the thermal treatment, whereas sheet resistance of FTO remained unchanged at the value of $8.5\,\Omega/\mathrm{sq}$. The cell based on ITO substrate has an overall cell efficiency of 2.24%; in contrast, an identical cell based on FTO has an efficiency of 9.6%. This experimental comparison correlating the sheet resistance to cell efficiency has confirmed that the ITO substrate is unstable when subjected to high temperature.

Although widely used, the traditional ITO and FTO based transparent conducting oxide appears to be increasingly problematic due to:

- the limited availability and high cost of the rare earth element indium,
- their sensitivity to thermal treatment and pH environment,
- their limited transparency in the near-infrared region, and
- mechanical brittleness [91].

Recently, ultrathin graphene films have been used in solid state DSCs as an alternative to ITO and FTO. As reported by Wang et al. [92], these graphene films obtained by reducing graphite oxide on the surface of the substrates show a high conductivity of 550 S/cm and a transmittance of more than 70% over 1000-3000 nm. Although cell efficiency based on graphene film is much lower (0.26%) than that of FTO-based cells, there are still several favorable characteristics that indicate graphene as a promising candidate, such as the outstanding chemical and thermal stability, and ultrasmooth surface with tunable wettability [93].

2.6. Theoretical and Modelling Considerations

2.6.1. Beer-Lambert's Law

The probability or rate of absorption is given by the Lambert-Beer Law. The Lambert law states that the fraction of incident radiation absorbed by a transparent medium is independent of the intensity of incident radiation and that each successive layer of the medium absorbs an equal fraction of incident radiation. The Beer law states that the amount of radiation absorbed is proportional to the number of molecules absorbing the radiation that is the concentration of the absorbing species.

Beer-Lambert's law is valid when: (i) the plot of absorbance vs concentration in the calibration graph is a straight line passing through the origin, (ii) the light of a single wavelength used, and (iii) the solution contains only one species capable of absorbing that particular

wavelength. As a first approximation the absorption of the dye can be described with Beer-Lambert's Law:

$$\frac{I(x)}{I_0} = 10^{-\alpha(\lambda)\cdot x\cdot C_{dye}} \tag{2.16}$$

where $I(x)$ is light intensity at point x; I_0 is initial light intensity; α is absorption coefficient; λ is wavelength; C_{dye} is dye concentration; and x is distance.

2.6.2. Metal-Semiconductor Contact

As ITO glass is highly doped material, its contact with TiO_2 semiconductor layer can be described by metal-semiconductor Shottky barrier junction. The current flows in a Schottky barrier because of charge transport from the semiconductor to the metal or in reverse direction. There are four different mechanisms by which the carrier transport can occur: (a) thermionic emission over the barrier, (b) tunneling through the barrier, (c) carrier recombination (or generation) in the depletion region, and (d) carrier recombination in the neutral region of semiconductor. Process (a) is usually the dominant mechanism, while (b) and (c) cause departure of the ideal behavior [94]. In thermal equilibrium situation, energy band diagram is illustrated as Figure 11.

Φ_m, Φ_n is the work function of metal and semiconductor repectively. In the metal there are electrons at the Fermi level E_{Fm}, but in the semiconductor there are non at E_{Fn}. Electrons tunneling from the semiconductor leave behind an electron-depleted region of width W in which there are exposed positively charged donors. The contact, called the built-in potential V_0.

The current due to electrons being thremally emitted from the metal to the conduction band (CB) of the smiconductor is

$$j_1 = C_1 \exp(\frac{\Phi_B}{kT}) \tag{2.17}$$

where C_1 is some constant, whereas the current due to electrons being thermally emitted from the CB of the semicondutor to the metal is

$$j_2 = C_2 \exp\left(\frac{eV_0}{kT}\right) \tag{2.18}$$

where C_2 is some constant different than C_1.

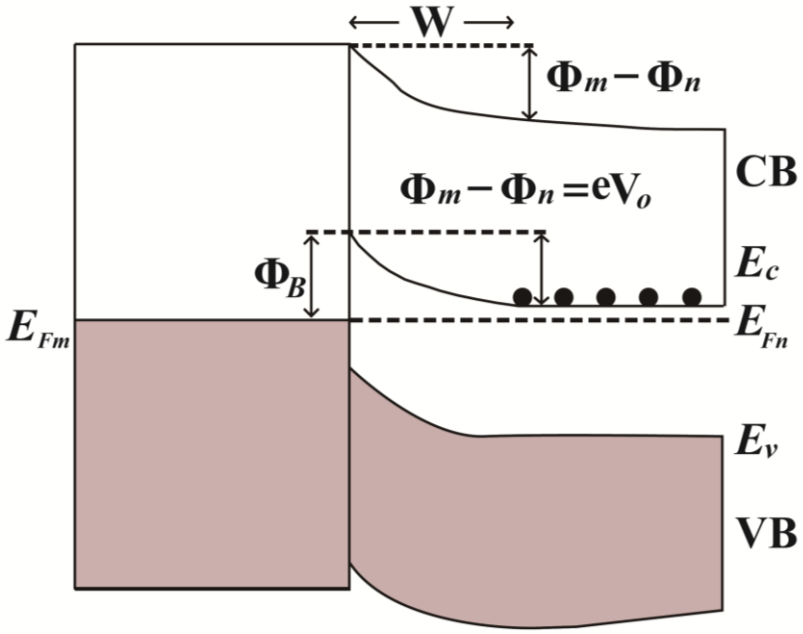

Figure 11. Formation of a Schottky junction between a metal and an n-type semiconductor.

In equilibrium, open circuit conditions in the dark, the currents are euqal but in the reverse directions:

$$j_2 - j_1 = 0 \tag{2.19}$$

Under forward bias conditions, the applied bias is in the opposite direction to the built-in voltage V_0, V_0 is reduced to $V_0 - V$.

The current j, due to electron emission from the semiconductor to the metal, is now

$$j_2^{for} = C_2 \exp\left(\frac{e(V_0 - V)}{kT}\right) \tag{2.20}$$

Since Φ_B is the same, J_1 remains unchanged. The net current is then

$$j_2^{for} - j_1 = C_2 \exp\left(\frac{e(V_0 - V)}{kT}\right) - C_2 \exp\left(\frac{eV_0}{kT}\right) \tag{2.21}$$

or

$$j = C_2 exp\left(\frac{eV_0}{kT}\right)\left[\exp\left(\frac{eV}{kT}\right) - 1\right] \tag{2.22}$$

leading to

$$j = j_0\left[\exp\left(\frac{eV}{kT}\right) - 1\right] \tag{2.23}$$

where j_0 is a constant that depends on the material and surface properties of the two solids.

2.6.3. Mass Transfer by Migration and Diffusion

Mass transfer in solution occurs by diffusion, migration, and convection [95]. Diffusion and migration result from a gradient in electrochemical potential, $\bar{\mu}$. Convection results from an imbalance of forces on the solution. Quantitative relation is given by Nernst-Planck equation:

$$j_{\mathrm{i}}(x) = -D_{\mathrm{i}}\boldsymbol{\nabla}\mathrm{C_i} - \frac{z_{\mathrm{i}}F}{RT}D_i C_i \boldsymbol{\nabla}\phi + C_i\boldsymbol{v} \tag{2.24}$$

Where D_{i} is the diffusivity of the chemical species, $\mathrm{C_i}$ is the concentration of the species, z_{i} is the valence of ionic species, $\boldsymbol{v}$ is the velocity of the fluid, and F is the Faraday constant. Under quiescent condition, that is in an unstirred or stagnant solution with no density gradients, the solution velocity, $\boldsymbol{v}$, is zeros, and the general flux equation for species i, Eq. (2.24) becomes

$$j_{\mathrm{i}}(x) = -D_{\mathrm{i}}\boldsymbol{\nabla}\mathrm{C_i} - \frac{z_{\mathrm{i}}F}{RT}D_i C_i \boldsymbol{\nabla}\phi \tag{2.25}$$

For linear mass transfer, this is

$$j_{\mathrm{i}}(x) = -D_{\mathrm{i}}\left(\frac{\partial \mathrm{C}_{\mathrm{i}}(x)}{\partial x}\right) - \frac{z_{\mathrm{i}}F}{RT}D_i C_i\left(\frac{\partial \phi(x)}{\partial x}\right) \tag{2.26}$$

where the terms on the right-hand side represent the contribution of diffusion and migration, respectively, to the total mass transfer. The mobility of species i, is linked to the diffusion coefficient by the Einstein-Smoluchowski eqution:

$$\mu_{\mathrm{i}} = \frac{|z_i|FD_i}{RT} \tag{2.27}$$

2.6.4. Butler-Volmer Derivation to Describe Interfacial Current

The I_2 reacts with the disassociated iodide ion, I^-, to produce triiododide (I_3^-) at electrolyte/platinum interface. Hauch and Georg [96] proposed the following reaction mechanism in acetonitrile solution:

(a)	$I^- + Pt \rightleftharpoons I^-(Pt)$	(adsorption of I^- fast on Pt) fast
(b)	$I^-(Pt) \rightleftharpoons I(Pt) + e$	(oxidation of I^-) slow
(c)	$I(Pt) + I(Pt) \rightleftharpoons I_2 + 2Pt$	(production of I_2) fast
(d)	$I_2 + I^- \rightleftharpoons I_3^-$	(production of I_3^-) fast

Pt is known to be an excellent catalyst for adsorption and dissociation processes as in step (c). The symbol $I^-(Pt)$ here does not mean only direct adsorption onto the Pt surface, but also includes the possibility that the I^- ion is still surrounded by a sphere of solvent molecules, so that the electrode by a tunnel process.

Iodide I^- is the reduced species of both the total reaction and the charge-transfer reaction. In contrast to this triiodide I_3^- is the oxidized species of the total reaction, but elementary iodine I

is the oxidized species of the charge-transfer reaction. Reaction (c) and (d) are fast chemical reactions, which are assumed to be always in equilibrium. The mass action law can be applied:

$$k_f[I][I] = k_b[I_2]$$

$$k'_f[I_2][I^-] = k'_b[I_3^-]$$

Using an appropriate equilibrium constant K, the concentration of elementary iodine $[I]$ at any point x in the effective medium is coupled with the concentration of iodide ($[I^-]$) and triiodide ($[I_3^-]$)

$$[I] = K[I_3^-]^{\frac{1}{2}}[I^-]^{-\frac{1}{2}}$$

2.7. Steady-State Photovoltaic Characterization

The overall performance of the above described solar cell can be evaluated in terms of cell efficiency (η) and fill factor (FF) expressed as:

$$FF = \frac{V_{max} J_{max}}{V_{oc} J_{sc}} \tag{2.28}$$

$$\eta = \frac{V_{oc} J_{sc} FF}{P_{in}} \times 100\% \tag{2.29}$$

where J_{sc} is the short-circuit current density ($mA\ cm^{-2}$), V_{oc} the open-circuit voltage (V), and P_{in} the incident light power. $J_{\max}$ and V_{max} correspond to current and voltage values where the maximum power output is given in the J-V curve.

To improve the overall conversion efficiency (η), most prominent influencing parameters such as V_{oc}, J_{sc}, and FF can be calculated for a given incident light intensity. In band gap theory, the difference between the quasi-Fermi level of the TiO_2 layer and the electrolyte redox potential determines the maximum voltage generated under illumination. As shown in Eq. (2.30) the open-

circuit voltage varies with the iodide concentration because the recombination reaction occurs between the electrons on the conduction band of TiO_2 and I_3^- (triiodide) [97].

$$V_{oc} = \frac{kT}{q}\ln\left(\frac{\eta\Phi_0}{n_0 k_{et}[I_3^-]}\right) \tag{2.30}$$

where η is the quantum yield of photogenerated electron for the given incident photo flux (Φ_0); n_0, represents the electron density on the conduction band of TiO_2 in the dark, while k_{et} reflects the recombination reaction rate for the given triiodide concentration $[I_3^-]$.

Similarly, the precise value of J_{sc} can be calculated by integrating the product of incident photon to current efficiency (IPCE) and incident photo flux (Φ_0) over the spectral distribution, expressed as:

$$J_{sc} = e\int IPCE(\lambda)\Phi_0(\lambda)\big(1 - r(\lambda)\big)d\lambda \tag{2.31}$$

where 'e' is the elementary charge and $r(\lambda)$ is the incident light loss. One prominent approach to improve the circuit current density (J_{sc}) is to increase the IPCE value by utilizing panchromatic dyes which can absorb incident light at a longer wavelength.

Yet another parameter that influences the efficiency of the DSC is the fill factor (FF) which is associated with the electron transfer process and internal resistance of dye-sensitized solar cells. A variety of equivalent circuits have been elaborated to interpret data obtained from electrochemical impedance spectroscopy [98, 99]. Based on the equivalent circuit study, it is shown that FF can be optimized by minimizing internal series resistance.

3. AIMS AND OBJECTIVES

The primary aim of this study is to develop a mathematical model which could simulate the charge transfer and charge transport within the nanoporous anode of the DSC under illumination. The anode of the DSC is considered to be the dye-sensitized nanoporous semiconductor film. It is intended to investigate loss mechanisms and charge transport process through simulation, and also validate the predicted results with experimental data as well as the numerical results published in the literature. Specific objectives of the mathematical model of this thesis include:

- To develop a model framework for the Semiconductor-dye-electrolyte interface within a DSC. This general framework will include all interfacial charge-transfer reactions. The reaction equations developed will account for the interactions within adsorbed dye molecules, electrons from the semiconductor as well as electrolyte species.
- To develop a comprehensive electrical model of charge transport within the porous anode of the DSC. This model will consist of mass transport within the semiconductor layer and electrolyte phase that comprises the nanoporous anode. Also, it would account for the porous nature of the anode and for charge transport via diffusion and migration. The model is expected to provide an insight into the contributions of charge transport to cell current and loss mechanisms of the DSC.
- The interfacial model and the charge transport model will be integrated together to analyze overall performance of the system. The numerical code comprising of non-linear differential equations, describing the entire DSC system, would be developed. It will employ “relaxtion method” to solve the two coupled components of the model.

4. THEORETICAL MODELING OF DYE-SENSITIZED SOLAR CELLS

4.1. Diffusion Model

4.1.1. Introduction

On the annual basis, North Dakota receives about 60 percent of total possible sunshine hours [100] (i.e., sufficient for the application of photovoltaic device). However, the large temperature variations between summer and winter conditions have long presented a challenge in design and implementation of dye-sensitized solar cells. The objective of this research is to investigate the influence of ambient temperature variation on the performance of dye-sensitized solar cells. In this paper, a theoretical model integrating a thermionic emission model into a diffusion model is developed to evaluate the device performance under extreme weather conditions. The results of the theoretical simulation are compared with experimental data. The details of the theoretical modeling and parametric analysis are discussed as follows.

4.1.2. Mathematical Modeling

In theory, the maximum voltage generated in DSCs is determined by the difference between the quasi-Fermi level of the TiO_2 and the redox potential of the electrolyte, about 0.7 V, e.g. the open-circuit voltage under solar illumination conditions. However, the voltage loss at the TiO_2/TCO interface should be taken into account in practical cases where such loss is not negligible in magnitude. Therefore, the reference photovoltage can be calculated as,

$$V = V_0 - V_1 \tag{4.1}$$

where V_0 is the potential difference between quasi-Fermi level of TiO_2 (E_{F}) and the redox potential of electrolyte (E_{redox}), and V_1 is the voltage loss at the TiO_2/TCO interface.

Under steady-state conditions of irradiated dye-sensitized solar cells, transport of the photoinjected electrons in TiO_2 mesoporous films can be described by the diffusion model [101]. In this simple diffusion model, two assumptions were proposed: (i). electrons are transported via diffusion. (ii). diffusion length is constant; i.e. recombination process is assumed to be of first order. Hence, the governing equation can be expressed as,

$$Dn''(x) - \frac{n(x) - n_o}{\tau} + \Phi\alpha e^{-\alpha x} = 0 \tag{4.2}$$

where D is the diffusion constant of the electrons in the film, $n(x)$ the excess electron density, n_0 the electron density in the dark ($n_0 = 10^{16}\ cm^{-3}$), $\tau$the electron lifetime, Φ the incident light intensity, and α the reciprocal absorption length.

Under short-circuit conditions, the electrons at the TCO/TiO_2 interface are efficiently drawn off as a photocurrent, and electrons reaching the outermost part of the film $x = d$ will be reflected and will diffuse back into the inner layers of the film (i.e. negligible current flow at $x = d$). The boundary conditions for substrate/electrode illumination are:

$$n(0) = n_o \tag{4.3}$$

and

$$\left(\frac{dn}{dx}\right)_{x=d} = 0 \tag{4.4}$$

The analytical solution of the short-circuit current density j_{sc} can be expressed:

$$j_{sc} = \frac{\left[\ -L\alpha\ cosh(\frac{d}{L}) + sinh(\frac{d}{L}) - L\alpha e^{-d\alpha}\right] L\alpha q\Phi}{(1 - L^2\alpha^2)cosh(\frac{d}{L})} \tag{4.5}$$

where q is the elementary charge of electron equal to $1.6 \times 10^{-19}\ C$; L is the electron diffusion length equal to $\sqrt{D\tau}$; and d is the thin film thickness.

When dye-sensitized solar cells operate under illumination, electron density in the conduction band of TiO_2 is increased to n as one boundary condition and another boundary holds as Eq. (4.3).

$$n(0) = n \tag{4.6}$$

Solving the diffusion equation with these boundary conditions gives the photocurrent as,

$$j = j_{sc} - \frac{qDn_0}{L} tanh\left(\frac{d}{L}\right)(e^{\frac{qV}{kTm}} - 1) \tag{4.7}$$

Rearranging Eq. (4.7) yields the expression for the voltage as a function of the photocurrent, i.e. the j-V characteristics.

$$V_0 = \frac{kTm}{q} ln(\frac{L(j_{sc} - j)}{qDn_0\, tanh\left(\frac{d}{L}\right)} + 1) \tag{4.8}$$

where k is the Boltzmann constant equal to $1.38 \times 10^{-23}\, m^2 kgs^{-2}K^{-1}$, and m is the ideality factor equal to 4.5.

Since TCO substrate is a high doped semiconductor or metal, their contact with TiO_2 can be simulated with Schottky barrier model [102]:

$$j = A^* T^2 exp(-\frac{\phi_b}{kT})(exp\left(\frac{qV_1}{kT}\right) - 1) \tag{4.9}$$

and

$$A^* = \frac{4\pi m^* q k^2}{h^3} \tag{4.10}$$

where h is the Planck constant equal to $6.626 \times 10^{-34}\, m^2 kg\, s^{-1}$, m^* is effective electron mass equal to 5.6 times the electron mass m_e [103], A^* is the Richardson constant of TiO_2 equal to $6.71 \times 10^6\, Am^{-2}K^{-2}$, and ϕ_b is the Schottky barrier height. The voltage loss can be expressed as a function of photocurrent.

$$V_1 = \frac{kT}{q} ln(1 + \frac{j}{A^* T^2 exp(-\frac{\phi_b}{kT})}) \tag{4.11}$$

The j-V relationship is obtained by substituting Eq. (4.11) and Eq. (4.8) into Eq. (4.1).

$$V = \frac{kTm}{q} ln\left(\frac{L(j_{sc} - j)}{qDn_0 \, tanh\left(\frac{d}{L}\right)} + 1\right) - \frac{kT}{q} ln(1 + \frac{j}{A^* T^2 exp(-\frac{\phi_b}{kT})}) \tag{4.12}$$

Performance parameters such as cell fill factor (FF) and cell efficiency (η) were calculated using the following equations:

$$FF = \frac{V_{max} \, j_{max}}{V_{oc} \, j_{sc}} \tag{4.13}$$

$$P_{max} = V_{max} \times j_{max} \tag{4.14}$$

where j_{sc} is the short-circuit current ($mA \, cm^{-2}$), V_{oc} the open-circuit voltage (V), and P_{max} the maximum power output. j_{max} and V_{max} are corresponding to current and voltage values where the maximum power output is reached in j-V curve.

Table 1. Primary simulation parameters used in integrated diffusion model.

Parameter	Value	Ref.
Light intensity, Φ ($cm^{-2} \, s^{-1}$)	1.0×10^{17}	
Light absorption coefficient, α (cm^{-1})	5000	[104]
Electron lifetime, τ (ms)	10	[105]
Ideality factor, m	4.5	[104]
Electron diffusion coefficient D ($cm^2 s^{-1}$)	2.3×10^{-5}	[107]
Richardson constant A^* ($Am^{-2}K^{-2}$)	6.71×10^6	[105]
Electron concentration in dark condition n_0 (cm^{-3})	10^{16}	[106,107]

4.2. Electrical Model

4.2.1. Model Assumptions

Much effort has been exerted to build models to simulate the working principle of dye-sensitized solar cells. Effective design of new device structure and its optimal performance is possible only by understanding the underlying mechanism. Sodergren et al. [101] presents a simple diffusion model of semiconductor films, which was based on two assumptions: (i) electron transport via diffusion only and (ii) the diffusion length is constant; i.e. recombination process is assumed to be of the first order. The governing equation used to describe electron transfer in semiconductor films can be expressed as:

$$Dn''(x) - \frac{n(x) - n_o}{\tau} + \Phi\alpha e^{-\alpha x} = 0 \tag{4.15}$$

where D is the diffusion constant of the electrons in the film, $n(x)$ the excess electron density, n_o is the electron density in the dark, Φ represents the incident light intensity, and α is the reciprocal absorption length. The solved I-V characteristic equation was similar to the expression for a p-n junction solar cell, but the properties of the electrolyte were not taken into account.

Later, Cao et al. [108] adopted this model to analyze the transient response of the cell and extended the diffusion coefficient as a function of the light intensity. However, the model only accounted for the production of electrons under illumination by a Beer-Lambert's Law [109]. Papageorgiou et al. [110] investigated the electrolyte mass transport in thin layer nanocrystalline photoelectrochemical solar cells, and determined the concentration of the redox active species under steady state irradiation as a function of current density as well as location and direction of irradiation.

An improved simplified complete electrical model was presented by Ferber et al. [103] to evaluate the performance of DSC by accounting the properties of the electrons in TiO2 films as well as the charge transport in the electrolyte solution and redox processes at the counter electrode. The charge transport within the TiO_2 conduction band and the electrolyte system was described with continuity and mass transport equations, and the macroscopic electric field was calculated using Poisson's equation. This work proposes a simplified electrical model of dye-sensitized solar cells, based on the concepts developed by Ferber et al. [103]. Parametric simulations were conducted to analyze the effect of diffusion/drift, dye loading, and electrode thickness on DSC performance. Experimental evidence was acquired to quantitatively validate the model. Relaxation method [111] was used to solve differential equations, and in-house codes were developed (MATLAB) to evaluate the system's performance. The codes are considerably concise and the sub-functions had confirmed good extensibility.

The model in its present state is based on assumptions listed below:

- Due to the small size of the colloids (≈20 nm), band bending within a TiO_2 colloid is negligible.
- The steady-state electron transport can be described with sufficient accuracy using an effective diffusion constant or mobility.
- Effects of microscopic electric fields in the cell, screening effects, etc. are neglected. Only an effective macroscopic electric field due to inhomogeneous charge-carrier distributions in the illuminated cell is taken into account.
- Helmholtz layers and diffuse layers are neglected in steady state analysis.
- Light absorption is assumed to occur by the charge-transfer dye only. Neither spurious absorption by direct interband excitation of TiO_2 nor the absorption of triiodide in the blue spectral range is taken into account.

- The electron generation rate and the electron relaxation rate are assumed to be potential independent.
- Overpotential at the electrolyte/counter electrode is assumed to be negligible.

4.2.2. Electron Generation and Recombination

To illustrate the methodology of analysis and optimization of the selected cell design as well as operational parameters, a one-dimensional, pseudo-homogeneous medium model for steady state condition has been developed and the schematic of chosen configuration of dye-sensitized solar cell is depicted in Figure 12. Important components and working principles of the considered system are described in chapter 2.1 in detail.

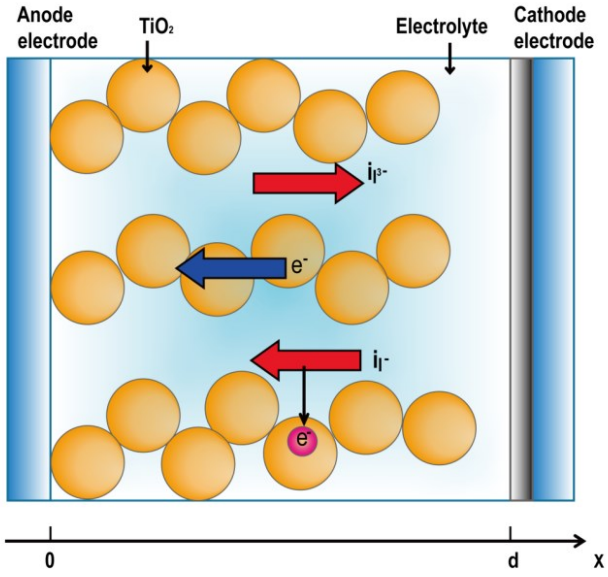

Figure 12. Schematic model for dye-sensitized solar cells.

When exposed to sunlight, the dye sensitizer gets excited, from which an electron is directly injected into the conduction band of the mesoporous oxide film (TiO_2). The generated electrons are then transported to the anode, which flow through an external load before neutralized by the electrolyte at cathode surface, to complete the cycle. Assuming steady state operation of

the cell, the characteristics of DSC is expressed in terms of the transport features of electron in TiO_2 semiconductor, I^- iodide and I_3^- triiodide redox medium in electrolyte solution, and the neutralizing counter cation.

Kinetics of the $RuL_2(NCS)_2$ dye sensitized TiO_2 solar cell with I^-/I_3^- redox mediator is schematically shown in Figure 13. The forward process 1, 2, and 3 denote the dye excitation, photogenerated electron injection, and dye regeneration, respectively. The back reaction a, b, and c refer to possible electron recombination routes. Previous experimental studies have shown that injection of the electron from dye molecule into TiO_2 conduction band occurs in the femtosecond time range which is much faster than the electron recombination with I_3^-.

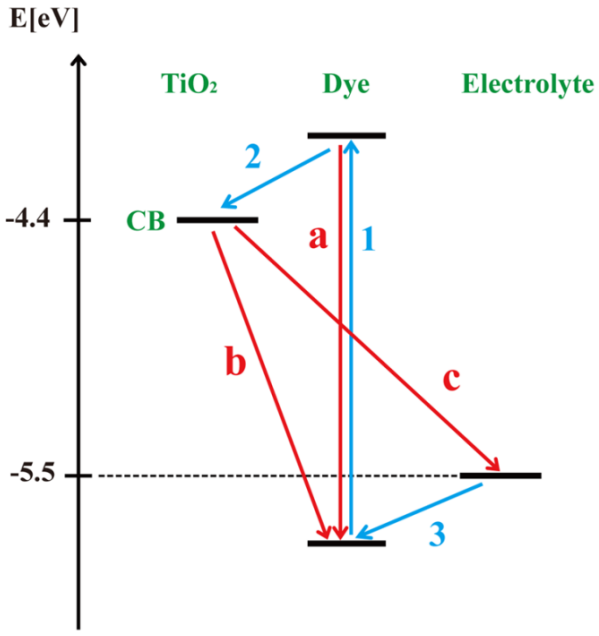

Figure 13. Kinetics of the $RuL_2(NCS)_2$ dye sensitized TiO_2 solar cell with I^-/I_3^- redox mediator.

In this study, a perfect electron injection is assumed and the electron generation rate $G_e(x)$ is expressed as [63]:

$$G_e(x) = \int \alpha(\lambda)\Phi(\lambda)e^{-\alpha(\lambda)x}d\lambda \tag{4.16}$$

where $\Phi(\lambda)$ is power flux obtained from standard solar radiation AM1.5 spectrum, reduced by reflectance and absorptance of TCO glass by 11% , and $\alpha(\lambda)$ is the light absorption coefficient of the sensitizing dye. $\alpha(\lambda)$ is defined as:

$$\alpha(\lambda) = \frac{\epsilon(\lambda)C_{dye}}{\log_{10} e} \tag{4.17}$$

where $\epsilon(\lambda)$ is molar extinction coefficient of sensitizing dye, and C_{dye} represents the absorbed dye concentration in the cell which is determined by the roughness factor of TiO_2 semiconductor.

In the presence of illumination, under steady state conditions the relaxation rate R_e of the conduction band electrons can be expressed as [6],

$$R_e = k_e \left\{ n_e \sqrt{\frac{n_{I_3^-}}{n_{I^-}}} - \bar{n}_e \sqrt{\frac{\bar{n}_{I_3^-}}{\bar{n}_{I^-}^3}} n_{I^-} \right\} \tag{4.18}$$

where k_e is the electron relaxation rate constant, n_e and $\bar{n}_e$ denote electron and equilibrium electron concentrations, respectively. n_{I^-}, $n_{I_3^-}$, $\bar{n}_{I^-}$, $\bar{n}_{I_3^-}$ are the respective concentration of iodide/triiodide and equilibrium iodide/triiodide solutions. At equilibrium, i.e. without illumination, the second term in the bracket would turn out to be negligible because of the low electron concentration in the dark.

4.2.3. Electron Transport

4.2.3.1. Continuity Equation

As electron combination rate R_e and electron generation G_e are defined, the continuity equation for current density for each species can be expressed as,

$$\frac{1}{e_0}\frac{dj_e}{dx} = R_e - G_e \tag{4.19}$$

$$\frac{1}{e_0}\frac{dj_{I^-}}{dx} = \frac{3}{2}G_e - \frac{3}{2}R_e = -\frac{3}{2e_0}\frac{dj_e}{dx} \tag{4.20}$$

$$\frac{1}{e_0}\frac{dj_{I_3^-}}{dx} = \frac{1}{2}R_e - \frac{1}{2}G_e = \frac{1}{2e_0}\frac{dj_e}{dx} \tag{4.21}$$

$$\frac{1}{e_0}\frac{dj_c}{dx} = 0 \tag{4.22}$$

where e_0 is the elementary charge.

4.2.3.2. Transport Equation

The current density j_e, j_{I^-}, $j_{I_3^-}$, j_c and electron density (n_e) satisfy the transport equation (Eqs 4.23, 4.24, 4.25, and 4.26) where D_e, D_{I^-}, $D_{I_3^-}$, and D_c presents the diffusion coefficients, while μ_e, μ_{I^-}, $\mu_{I_3^-}$, and μ_c presents the mobility of the individual charged species.

$$\frac{1}{e_0}j_e = D_e\frac{dn_e}{dx} + \mu_e n_e E \tag{4.23}$$

$$\frac{1}{e_0}j_{I^-} = D_{I^-}\frac{dn_{I^-}}{dx} + \mu_{I^-} n_{I^-} E \tag{4.24}$$

$$\frac{1}{e_0}j_{I_3^-} = D_{I_3^-}\frac{dn_{I_3^-}}{dx} + \mu_{I_3^-} n_{I_3^-} E \tag{4.25}$$

$$\frac{1}{e_0}j_c = -D_c\frac{dn_c}{dx} + \mu_c n_c E \tag{4.26}$$

Relation between the diffusion coefficient and mobility of the same charged species could be described using Einstein relation,

$$D = \frac{kT}{e_0}\mu \tag{4.27}$$

where k denotes the Boltzmann constant and T absolute temperature.

4.2.4. Poisson's Equation

Poisson's equation is a very useful mathematical relation for the calculation of electric fields and potentials that cannot be computed by using Coulomb's law and Gauss's law in electrostatic problems. According to the differential form of Gauss's law, the divergence of electric field E at any point is equal to $1/\epsilon_0$ times the volue charge density at that point. That is,

$$div\ E = \frac{\rho}{\epsilon_0} \tag{4.28}$$

The electric field may also be expressed as negative gradient of potential V. That is,

$$E = -grad\ V = \vec{\nabla} V \tag{4.29}$$

Substituting this value of E in Eq.4.28 , we obtain

$$div(-grad\ V) = \frac{\rho}{\epsilon_0} \tag{4.30}$$

$$\nabla^2 V = \frac{\rho}{\epsilon_0} \tag{4.31}$$

Eq. (4.31) is known as Poisson's equation for a homogenous region and the operator ∇^2 as Laplacian.

The electric field E built in the cell can be characterized using 1D Poisson's equation:

$$\frac{dE}{dx} = \frac{e_0}{\epsilon\epsilon_0}\left[n_c(x) - n_e(x) - n_{I^-}(x) - n_{I_3^-}(x)\right] \tag{4.32}$$

It is essential to have appropriate boundary conditions while solving a set of six coupled non-linear differential equations (one continuity equation, four transport equations and Poisson's equation) along with six independent variables (effective electric field, a current density of free electrons , and concentration of all four charged spices).

4.2.5. Boundary Conditions

Integral Boundaries: According to the law of conservation of the mass, the concentration of the cations and the number of the iodine nuclei are assumed to be constant, which yields the following three integral boundaries:

$$\int_0^d n_c \, dx = \int_0^d n_c^0 \, dx = n_c^0 \cdot d \tag{4.33}$$

$$\int_0^d (n_{I_3^-} + \frac{1}{3} n_{I^-}) \, dx = (n_{I_3^-}^0 + \frac{1}{3} n_{I^-}^0) \cdot d \tag{4.34}$$

$$\int_0^d (\frac{1}{2} n_e + \frac{1}{3} n_{I^-}) \, dx = (\frac{1}{2} n_e^0 + \frac{1}{3} n_{I^-}^0) \cdot d \tag{4.35}$$

An Upper index "0" denotes initial concentration. Because of the charge neutrality condition, equilibrium concentration will satisfy the following equation:

$$\int_0^d (n_e + n_{I^-} + n_{I_3^-}) dx = (n_e^0 + n_{I^-}^0 + n_{I_3^-}^0) \cdot d = n_c^0 \cdot d \tag{4.36}$$

It is noted that the initial concentration of iodide and triiodide have to be multiplied by the porosity (p) to obtain $n_{I^-}^0$ and $n_{I_3^-}^0$ in the pseudo-homogeneous medium.

Metal-Semiconductor Contact: As TCO substrate is a highly doped semiconductor or metal, their contact with TiO_2 is assumed to be ohmic, and no surface charge exists. Therefore,

$$E(0) = 0 \tag{4.37}$$

The movement of all the charged species is restricted within the inner cell, and hence the following conditions will be fulfilled:

$$j_c(0) = j_{I^-}(0) = j_{I_3^-}(0) = j_e(d) = 0 \tag{4.38}$$

$$j_e(0) = j_{int} \tag{4.39}$$

Voltage Conditions: In this study, overpotential at the electrolyte/counter electrode is assumed to be negligible. This assumption holds true in open-circuit condition, as well as at

maximum power point [96]. It should be pointed out that in practice, the overpotential may display a non-ideal behavior caused by the interactions between the particles in the electrolyte. For idealized conditions, the internal voltage of the electrochemical cell is calculated by:

$$U_{int} = \frac{1}{e_0}[E_F^n(0) - E_R(d)] \tag{4.40}$$

where U_{int} denotes cell's internal voltage, $E_R(d)$ represents the redox potential at counter electrolyte, and $E_F^n(0)$ denotes the Fermi-level of TiO_2 which could be determined based on the electron concentration $n_e(0)$ in the conduction band. The quantitative relationship is depicted using the following expression:

$$E_F^n(0) = E_{CB} + kTln\left(\frac{n_e(0)}{N_{CB}}\right) \tag{4.41}$$

where E_{CB} reflects the energy level of the conduction band edge and N_{CB} the effective density of states in the TiO_2 conduction band (Eq. 4.42).

$$N_{CB} = 2\left(\frac{2\pi m_e^* kT}{h^2}\right)^{\frac{3}{2}} \tag{4.42}$$

where m_e^* presents effective electron mass and h Planck's constant.

4.2.6. Relaxation Method

The set of six nonlinear coupled differential equations is extremely stiff, due to Poisson's equation. Because of the stiffness the solution being sought varies slowly, but there are nearly solutions that vary rapidly, so the numerical method must take small steps to obtain satisfactory results. Stiffness is an efficiency issue. If we were not concerned with how much time a computation takes, we would not concern about stiffness. Nonstiff methods can solve stiff problems; they just take a long time to do it. In this work, a relaxation method is proved to works well in solving the set of six nonlinear coupled differential equations.

In relaxation methods, we replace ordinary differential equations (ODEs) by approximate finite-difference equations (FDEs) on a grid or mesh of points that spans the domain of interest. Due to the variation by several orders of magnitude, particularly in the electron and triiodide concentrations and the sharp drop in the electrical field, more grid points was turned out to be necessary near the boundary ($x = d$) to make calculation feasible on personal computer. It should be noted that standard relaxation method is only applicable to boundary value problems, therefore integral boundary conditions has to be converted to boundary value condition before implementation. The detail transformation can be found in [103]. Figure 14 shows the procedure of implementing relaxation method. To begin the calculations, a trial solution (i.e. initial guess) consisting of values for the dependent variables at each mesh point, has to be substituted into the finite-difference equations.

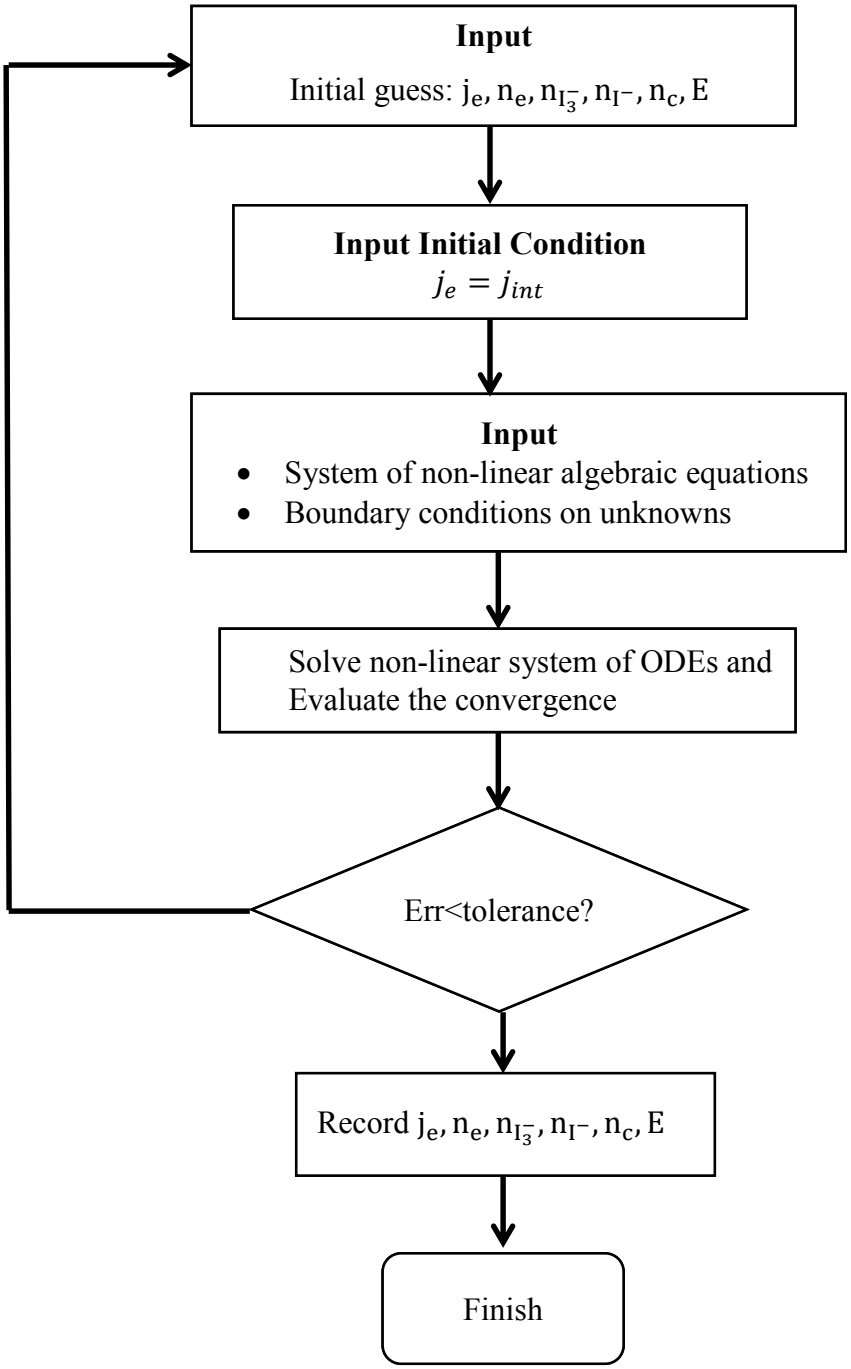

Figure 14 . Flow diagram of relaxation method iteration procedure.

5. SIMULATION RESULTS AND PARAMETIC STUDY

5.1. Diffusion Model

5.1.1. Model Validation

As it is shown in Figure 15, the predicted results using the model developed in this study agrees well with the experimental data obtained by M. Berginc et al [112], especially when I_2 concentration is lower than 0.09 M. Also, the results clearly reflect that low operating temperatures have an adverse effect on the performance of DSCs.

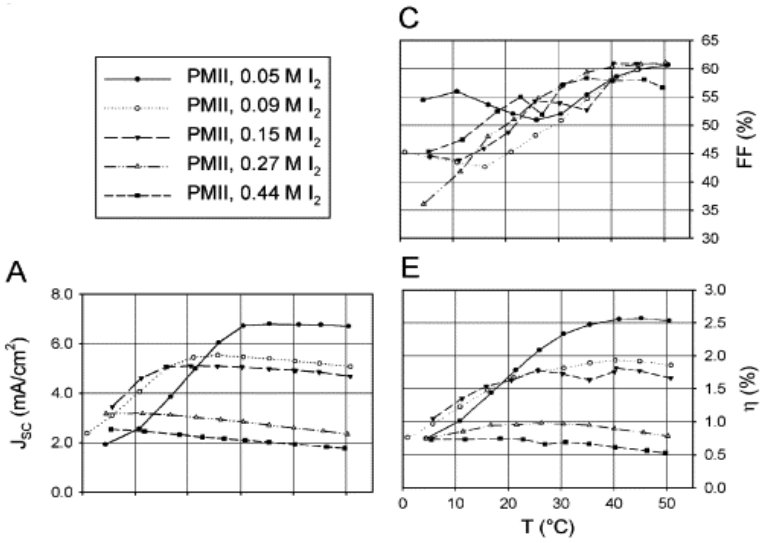

Figure 15. Effect of operating temperature on j_{sc} (A), fill factor (C) and efficiency (E) [112].

5.1.2. Results and Discussion

In dye-sensitized solar cells, the back reaction of electron from the conducting glass substrate to triiodide ions is an important loss mechanism especially at maximum power point and open circuit. Under an open circuit condition, the voltage loss at TCO/TiO_2 is determined by temperature, Schottky barrier height, and recombination current. The recombination current varied in a wide range depending on the material composition of TCO substrates and the existence

of a blocking layer. In this study, the recombination current density of value $J = 0.0001\ Am^{-2}$ was chosen [113]. At TiO_2/TCO interface, the voltage loss variation against temperature and Schottky barrier height is plotted in Figure 16.

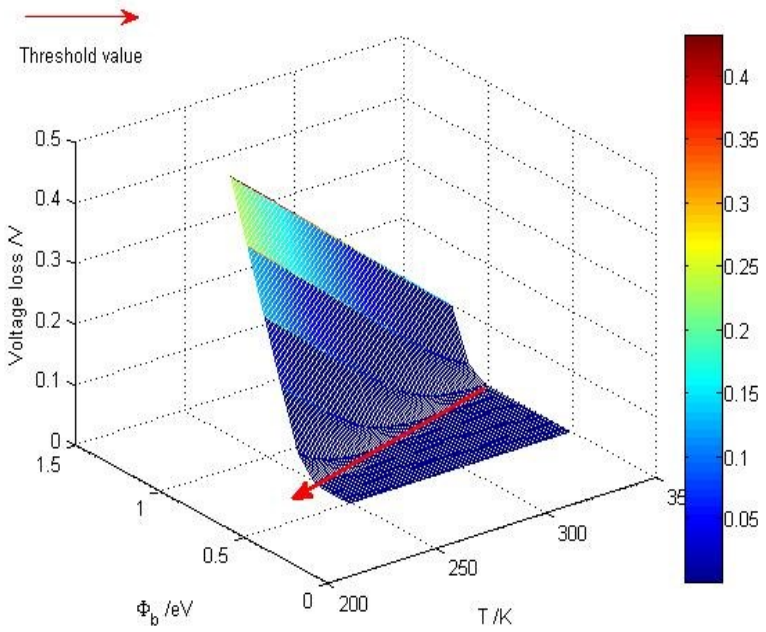

Figure 16. Variation of voltage loss at TiO_2/TCO contact with temperature and Schottky barrier.

It is found that lowering temperature results in an increase of voltage loss, and when ϕ_b value is beyond c.a. 0.6 eV a significant voltage loss occurs. Figure 16 shows (red line) that there exists critical threshold value. When the Schottky barrier height is below this critical value, the temperature effect on voltage loss is inappreciable and the voltage loss is negligible. This conclusion serves as a useful guide for TCO materials selection indicating lower ϕ_b is more suitable for obtaining higher open circuit voltage. These simulation results are consistent with the experimental studies, in which fluorine doped tin oxide ($\phi_b < 0.6\ eV$) was used as the TCO material [102].

Assuming $\phi_b = 0.6\,eV$, the open-circuit voltage (V_{oc}), maximum power output (P_{max}), and overall conversion efficiency (η) are calculated and listed in Table 2. The effect of temperature on DSC j-V characteristics is illustrated in Figure 17. It could be seen that, when temperature increases, the thermal energy also increases to excite more electrons from the valence band to the conduction band of TiO_2. This alleviates interfacial voltage losses resulting in a better device performance.

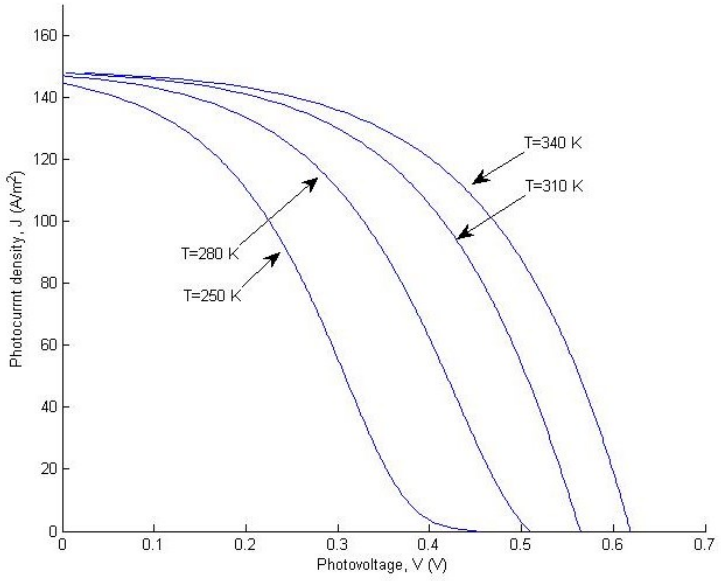

Figure 17. Effect of operating temperature on DSC J-V characteristics.

Table 2. Effect of the operating temperature on the performance of DSCs.

T	**V_{oc}**	**j_{sc}**	**FF**	**P_{max}**	**η**
K	V	mA cm^{-2}		W/m^2	%
250	0.45	14.83	0.33	22.57	2.26
280	0.51	14.83	0.44	33.21	3.32
310	0.56	14.83	0.51	42.57	4.26
340	0.62	14.83	0.53	48.61	4.86

The effect of operating temperature on DSC fill factor and maximum power output is plotted in Figure 18. It is found that both the fill factor and maximum power output increase simultaneously as the temperature increases. When the temperature is over 310 K, the fill factor tends to be steady. This phenomenon indicates that at high temperatures, the thermal energy influence on the DSCs' performance is attenuated.

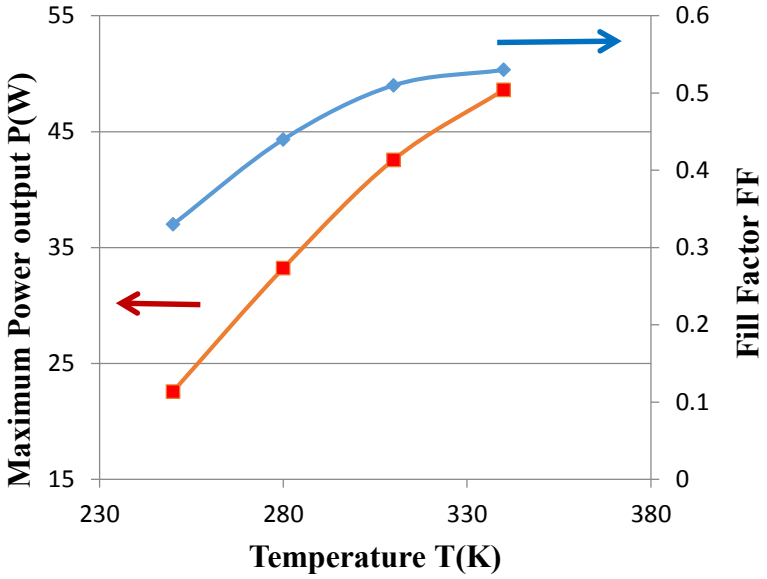

Figure 18. Effect of operating temperature on DSC fill factor (a) and maximum power output (b).

In this work, the extreme cold weather has proven to be detrimental on cells performance as well as on their service life because of the fact that electrolytes freeze rapidly, causing the system to fail—sometimes as even during sunny days. To maintain higher working temperature, two ways are suggested to efficiently utilize solar energy:

I. to design and fabricate an insulated cell-housing that is compatible with the regional environmental conditions.

II. to design and fabricate a mounting arm that could allow the panel to be inclined at an optimum tilt angle to maximize the incoming solar radiation.

5.1.3. Summary

A simple model of a DSC is derived which could predict the effect of temperature on performance factors such as voltage loss at TCO/TiO_2 interface and the j-V characteristics. The simulated results are in a good agreement with experimental data. The present study has shown that at low temperatures like -20 °C, the maximum power output drops to a value about half lower than that it could have attained at 70 °C, indicating the significance of operating temperature on the DSCs' performance particularly in extreme weather condition.

5.2. Electrical Model

5.2.1. Model Validation

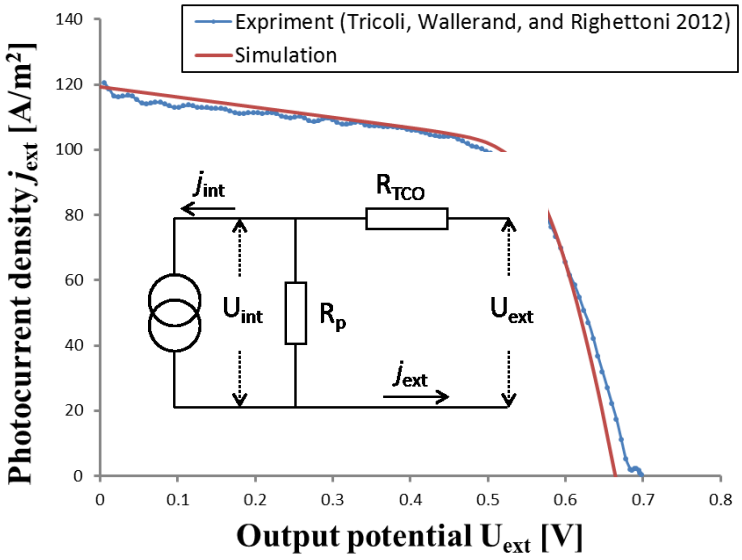

Figure 19. Validation of the present numerical model with the experimental results (Tricoli, Wallerand, and Righettoni 2012) [114]. The fit parameters of the calculated curve are: $R_p = 3.2\ k\Omega$, $R_{TCO} = 6\ \Omega$, thickness $d = 38\ \mu m$, porosity $p = 95\ \%$, $C_{I_3^-} = 0.6$ M, $C_{I^-} = 0.1$ M, dye N-719 concentration = 1.5×C_{dye}, other parameters as in Table 3.

To analyze the proposed electrical model, simulation of typical dye-sensitized solar cells has been carried out and the values of the basic input parameters are listed in Table 3.

Figure 19 shows the trend in photocurrent density and has been compared with experimental data reported by Tricoli *et al*. [114]. The experimental studies were conducted on an extremely high porous DSC ($\mathrm{p} = 95\%$) in combination with $C_{I_3^-} = 0.6\ M$, $C_{I^-} = 0.1\ M$, and N-719 dye. It was reported that such cell could attain an overall efficiency of about 5%. As shown in Figure 19, the j-V plot generated by the proposed model agrees reasonably well with the experimental data reported by Tricoli *et al*. However, there appears a discrepancy at the maximum power point, which reflects the fill factor (FF) value. This discrepancy is mainly caused by the influence of series-internal resistance which correlates positively with sheet resistance of the transparent conducting oxide and the thickness of the electrolyte layer whereas negatively with the roughness factor of platinum counter electrode [115]. In the experiment study, the tested DSC was thick (38 μm) and porous, the internal resistance of cell could have been suspected high which had resulted in low fill factor values [116].

Table 3. Base case parameters used for simulation of dye-sensitized solar cell.

Symbol	Value	Note
k_e	$10^4\ s^{-1}$	Electron relaxation rate constant
μ_e	$0.3\ cm^2/Vs$	Electron mobility
D_{I^-}	$8.5 \times 10^{-6}\ cm^2/s$	Iodide diffusion constant in nanotube
$D_{I_3^-}$	$8.5 \times 10^{-6}\ cm^2/s$	Triiodide diffusion constant in nanotube
C_{I^-}	$0.45\ M$	Initial concentration of iodide
$C_{I_3^-}$	$0.05\ M$	Initial concentration of triiodide
m_e^*	$5.6\ m_e$	Effective mass of electron
ϵ	50	Effective relative dielectric constant
$E_{CB} - E_{Redox}^0$	$0.93\ eV$	Difference of conduction band and standard electrolyte redox energy
d	$10\ \mu m$	Thickness of inner cell
A	$1\ cm^2$	Cell area
p	0.5	Porosity of TiO_2 semiconductor
R_f	1000	Roughness factor of TiO_2 semiconductor
T	$298\ K$	Temperature

5.2.2. Role of Electrical Field

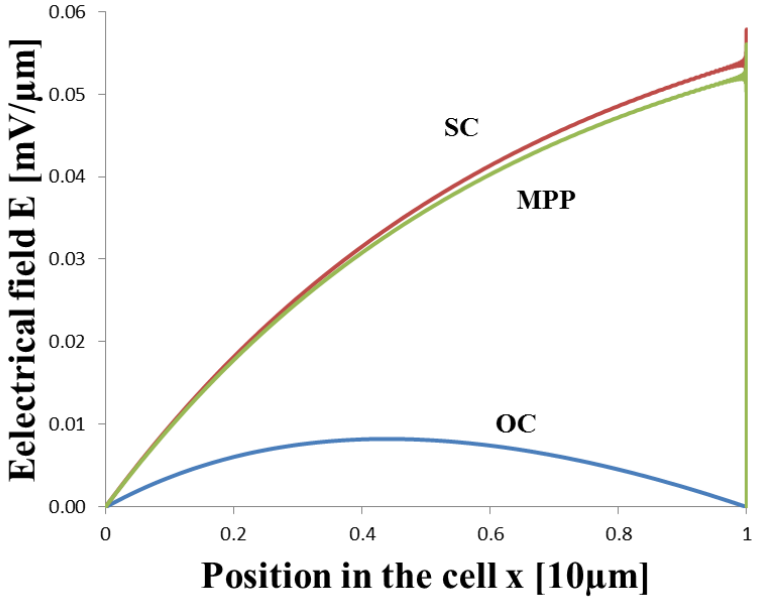

Figure 20. The distribution of the electric field within the modeled DSC under short-current (SC), maximum-power-point (MPP) and open-circuit (OC) conditions.

Having validated the proposed model, the model was used to predict the electrical field distribution (shown in Figure 20), which in general is influenced by the potential drop and the current density. It could be seen from Figure 20 that the macroscopic internal electrical field has been relatively small at maximum-power-point (ca. 0.05 $mV/\mu m$), corresponding to a potential drop less than 1 mV. This observation is consistent with the previous experimental results [117], substantiating the model validation. Similarly, the current density, more specifically the diffusion component of the current, influences the electric field distribution. However, with respect to the drift current although Usami [118] suggested drift current does influence energy conversion process, the study reported in this paper shows that the drift component in transport equation does not have a significant contribution to charged species' movement. This may be due to the fact that, as the contact of the TCO/TiO_2 interface is assume to be ohmic, there exists no surface charge at

the interface (x = 0) and therefore the electric field vanishes. Hence, the predicted drift current ($j_e = qn\mu E$) is reported to be zero at TCO/TiO_2 interface because of the absence of electric field.

5.2.3. Effect of Electron Mobility

One of the main parameters that characterize how spontaneously electrons can be transported through TiO_2 film is the "electron mobility". The influence of different magnitudes of electron mobility on j-V characteristics is shown in Figure 21.

It is observed that higher the electron mobility, higher is the short-circuit current and lower is open circuit voltage. That is, higher value of electron mobility implies a shorter transit time and less electron loss during recombination. Such short transit time in turn inhibits the accumulation of electrons in the TiO_2 semiconductor, and thus lowers the open-circuit potential of TiO_2 conduction band. Overall, only a marginal drop in potential is realized which will not affect performance of the DSCs. Besides titanium dioxide (TiO_2), other semiconductor materials such as Zinc oxide (ZnO), tin dioxide (SnO_2), and ternary oxides (Zn_2SnO_4) are promising alternatives which have higher electron mobility [119]. It is noticeable that apart from the intrinsic property of different materials, other factors such as particle size and fabrication techniques also affect the electron mobility. Aduda et al. [120] measured the drift mobility by time-of-flight technique for porous TiO_2. It is found that the drift mobility is dependent on the morphology of the film. Columnar TiO_2 film which was aligned along the electric field direction displayed higher drift mobility than random distribution of TiO_2 particles.

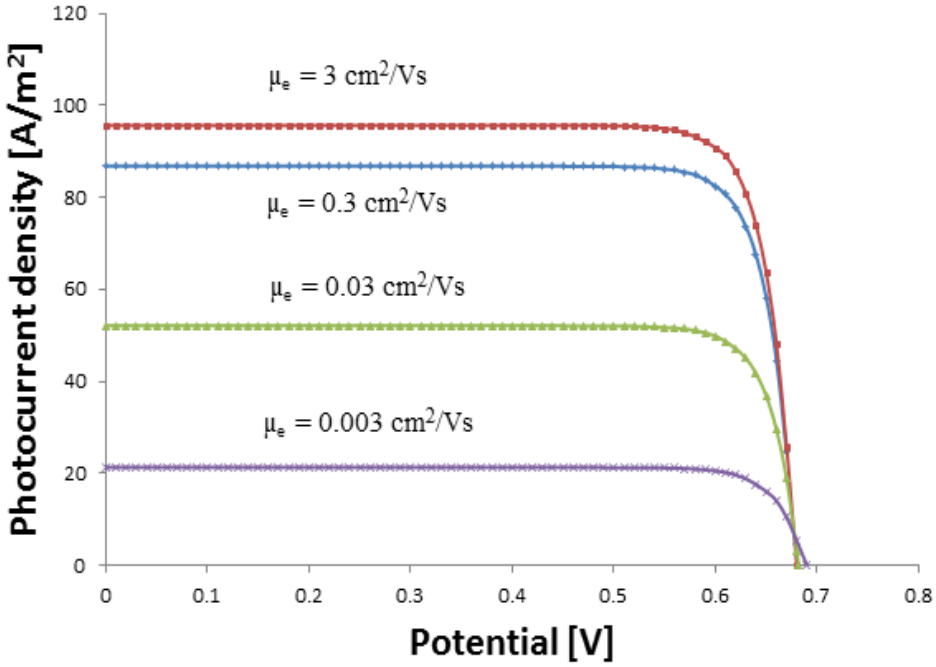

Figure 21. The influence of the electron mobility μ_e on the j-V curves.

5.2.4. Effect of Electrolyte Diffusion

The electrolyte plays a crucial role in dye-sensitized solar cells. It functions as charge carriers collecting electrons at the cathode and transporting the electrons back to the dye molecule. In this study, iodide/triiodide (I^-/I_3^-) based organic electrolyte is taken as the prototype to investigate the influence of diffusion coefficient on the overall conversion efficiency. The dependence of the energy conversion efficiency on the diffusion constants of redox ions is presented in Figure 22.

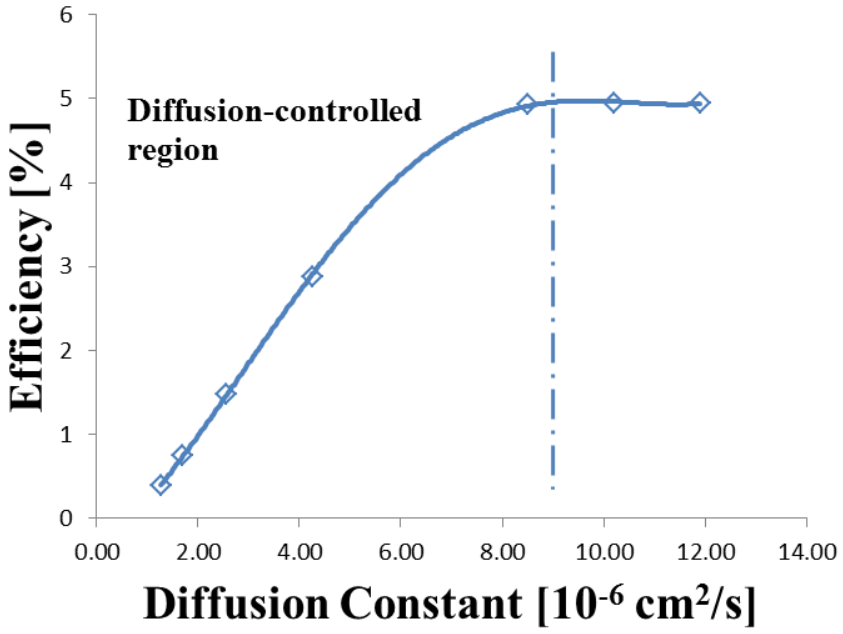

Figure 22. The dependence of energy conversion efficiency on the diffusion constants of redox ions.

It is seen that the efficiency increases with an increase in diffusion efficiency, and it reaches a threshold value at about $8.5 \times 10^{-6}\ cm^2/s$, beyond which it is interpreted that the diffusion constant is high enough, such that the diffusion process of redox couple could no longer be a limiting factor. This result serves as a standard and any other novel electrolyte either room temperature ionic liquids (RTILs), quasi-solid or solid state electrolyte need to meet the said standard in order to minimize the diffusion resistance. From the perspective of materials, the diffusion coefficient of electrolyte is generally influenced by redox couple concentration, viscosity of organic matrix, and the porosity of TiO_2 film. It is evident that high redox concentration, low solution viscosity, and high porosity favor high diffusion coefficient.

5.2.5. Design of Cell Thickness

Although the diffusion limit can be alleviated in a thin DSC by minimizing cell length, thin structure may deteriorate the cell efficiency due to insufficient dye uptake. Therefore, an optimized cell thickness is indispensable for maximizing device efficiency. In Figure 23, the dependence of the energy conversion efficiency on the cell thickness 'd' is depicted.

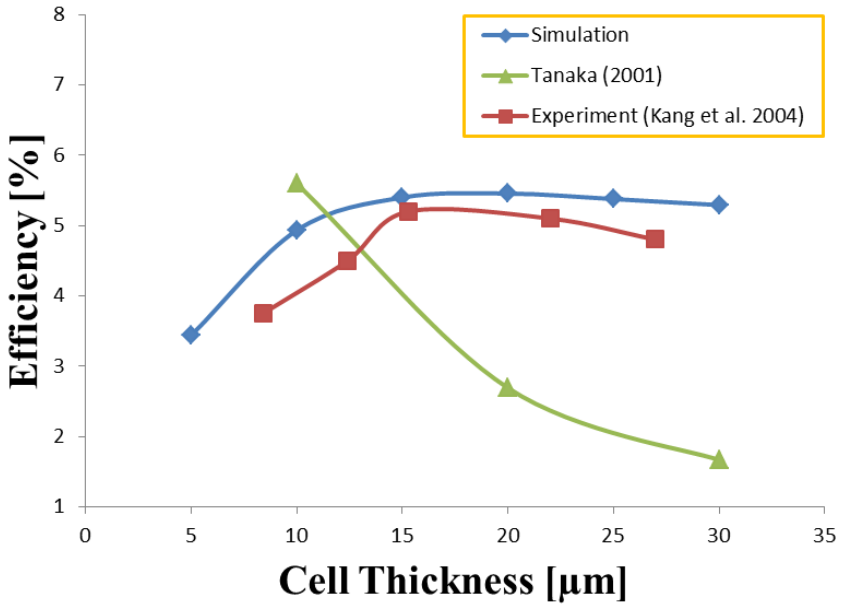

Figure 23. The dependence of energy conversion efficiency on the cell thickness. Solid diamonds: the present simulation results; solid triangles: simulation results of Tanaka (2001); solid squares: experimental results of Kang et al. (2004).

It is seen that the overall efficiency increases steadily with film thickness, reaching a maximum of 5.3 % at a thickness of 15 µm. Compared to the work of Tanaka [121], simulated results of the present study show a better agreement with the experimental data [122]. A wildly accepted fact suggests the less thickness becomes a constraint on photon absorption whereas large thickness causes a limitation on I^-/I_3^- ion diffusion and intensified recombination. Based on the simulation, though the optimized cell thickness can range between $10 - 15\ \mu m$, generally a standard

thickness of 10 µm is considered in DSC experimental studies. In this simulation, the thickness of counter electrode is not taken into account because the Platinum catalyst particle has an excellent performance so that a 2 nm thin film is sufficient to ensure a good cell performance [123].

5.2.6. Effect of Dye Uptake and Recombination Rate

Dye uptake is yet another factor that plays an essential role in the function of dye-sensitized solar cells. Figure 24 shows the effect of dye-adsorption on current density-voltage characteristics. It could be clearly seen that j_{sc} increases logarithmically with the amount of adsorbed dye sensitizer. Due to the cumulative increase in the generated electrons, the potential level of TiO_2 conduction band is also shown to rise up while in open circuit condition. The overall efficiency can be predicted with the following expression

$$\eta = \frac{V_{oc} j_{sc} FF}{P_{in}} \tag{5.1}$$

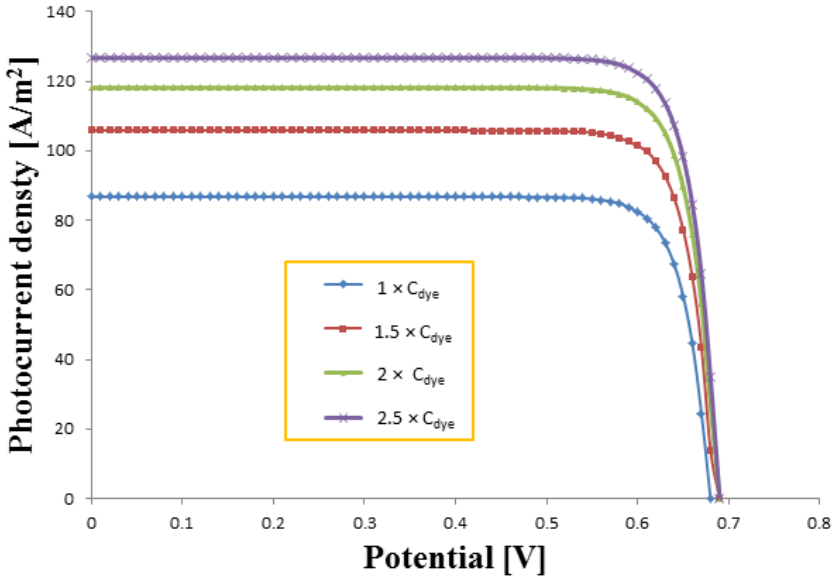

Figure 24. Dependence of the j-V characteristics on the amount of dye adsorption. Dye concentration is calculated as $C_{dye} = \sigma \times R_f / d_0$, $\sigma = 1.3 \times 10^{-10}\ mol\ cm^{-2}$, $R_f = 1000$, $d_0 = 10\ \mu m$.

In summary, an increase in the amount of the dye sensitizers can simultaneously increase the short circuit current and the open circuit voltage, effecting better cell performance. Therefore, research focus is directed towards identifying high porous materials with more surface area, and different morphologies that has better uptake ability of more dye molecules. Increase in photogenerated electrons will inevitably intensify the recombination which has been proven in the proposed electrical model on DSC. Based on the present study, it is found that high recombination rate (k_e) strongly affects the open circuit as well as short circuit current (Figure 25). Therefore, a careful consideration is required when experimentalists decide the possible matchup between semiconductor materials and electrolyte redox mediator.

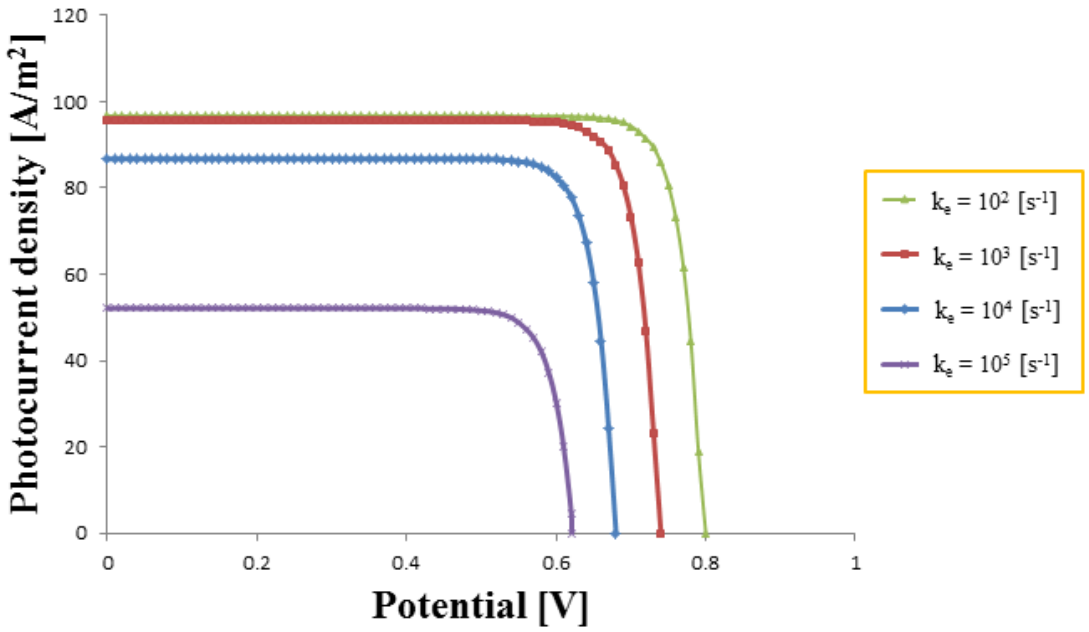

Figure 25. The dependence of energy conversion efficiency on the recombination reaction rate k_e.

6. CONCLUSIONS & FUTURE RESEARCH

A surge in fuel price over the last decade has become a major driving force for developing renewable technology. Dye-sensitized solar cells provide a high efficiency, low cost, and long-term stable alternative to the silicon-based conventional solar cells. Since its invention in the early 1990s [8], significant research efforts have been exerted to study the physical process within its regenerative photoelectrochemical system [26]. To further increase the efficiency, a detailed quantitative physical model is indispensable in optimization of various operating parameters and cell configurations.

In the first part of this thesis, a simple diffusion model of a DSC is derived which could predict the effect of temperature on performance factors such as voltage loss at TCO/TiO_2 interface and the j-V characteristics. The simulated results are in a good agreement with experimental data. It has shown that at low temperatures like -20 °C, the maximum power output drops to a value about half lower than that it could have attained at 70 °C, indicating the significance of operating temperature on the DSCs' performance particularly when exposed to extreme weather conditions.

In the second part, a comprehensive electrical model of dye-sensitized solar cell based on continuity, transport and Poisson's non-linear differential equations has been successfully presented. The simulated results have proven that diffusion is the major driving force for electron and ion transport, while the drift of electrons is negligible, which justifies the assumption made in the diffusion model. This simplified boundary condition improves the numerical calculation efficiency without deteriorating the accuracy of the model. The effects of the sensitizing dyes, TiO_2 meso-structure and I^-/I_3^- electrolyte on the j-V characteristics were simulated and there exists a good agreement between the predicted overall conversion efficiency and experimental results. Dependence of the cell performance on various input parameters (e.g. electron mobility,

diffusion coefficient, and recombination rate) was analyzed. The simulated optimal thickness was found to be consistent with the published results in the literature. Hence, this model possesses a good feature: it can be extended to cover more dedicated parametric analyses and detailed working principle in exhaustive cell components.

6.1. Future Research

A number of extensions to the modeling work are possible, which could improve the predictive qualities of the electrical models developed in this work and enable further investigations of loss mechanism within the DSC.

An obvious extension to the modeling work is to explicitly include individual components of the DSC system such as transparent conducting glass, electrolyte-platinum contacts, electrolyte-TCO contacts, and semiconductor-TCO contacts. The loss mechanism related to those components can be modeled based on a simple equivalent circuit model. By including these components through charge transport and interfacial kinetics modeling, the extended model would provide better accuracy in predicting the individual components' contribution to current generation and efficiency of the DSC.

Alternatively, the one-dimensional model presented in this thesis could be extended as a two-dimensional model, which would take into account of double layer effects. In addition, the two-dimensional model would provide the possibility of modeling individual particle effects such as surface conductivity, electron tunneling and electron movement through surface and bulk traps, on the overall DSCs' performance.

Interfacial model could be refined by including trap states, or a distribution of a trap states, at the surface of the semiconductor particles. This extension would require appropriate interfacial kinetic values for the additional reactions at the interface. Such extension also suggests

augmentation of the governing equations, in which charge transport in the semiconductor includes electron movement in traps. These charge trapping and detrapping behavior could be simulated by the use of random walk models.

Further extension of the model could include investigation on the transient response of the cell. The model equations presented in this study could be further extended to include the rate of change for each differential equation. However, careful consideration would be required to determine the time step size in the numerical algorithm which must account for unltrafast injection from excited dye molecules. In addition, the system of governing equations is expected to be extremely stiff, so not only is the time step size important but also the choice of numerical solver/algorithm.

Additionally, the presented electrical model could be used to investigate other dye complex by using appropriate interfacial kinetic values or to investigate different electrolyte systems and semiconductor materials by using the appropriate diffusion and material specific parameters. Moreover, the electrical model proposed in this thesis could be used as a base-model for DSC designs that incorporates an organic hole conduction materials, as opposed to conventional electrolyte systems.

REFERENCES

[1] http://www.energy.eu/

[2] http://www.whitehouse.gov/issues/energy-and-environment

[3] H. Nobuyuki. Renewable energy: RD & D priorities: insights from IEA technology programmes (2006)

[4] REN21. Renewables 2010 Global Status Report

[5] M.A. Hasan, K. Sumathy. Photovoltaic thermal module concepts and their performance analysis: A review, Renewable and sustainable energy reviews 2010; 14(7): 1845-1859.

[6] H. Hoppe, NS. Sariciftci. Organic solar cells: An overview, Journal of Materials Research 2004; 19(7): 1924-1945.

[7] S. Günes, H. Neugebauer, N.S. Sariciftci. Conjugated polymer-based organic solar cells Chemical Reviews 2007; 107(4): 1324-1338.

[8] B. O'Regan, M. Gratzel. A low-cost, high-efficiency solar cell based on dye-sensitized colloidal TiO2 films, Nature 1991; 353: 737-740.

[9] F, Gao, Y. Wang, D. Shi, J. Zhang, M. Wang, X. Jing et al. Enhance the optical absorptivity of nanocrystalline TiO_2 film with high molar extinction coefficient ruthenium sensitizers for high performance dye-sensitized solar cells, Journal of the American Chemical Society 2008; 130(32): 10720-10728.

[10] http://en.wikipedia.org/wiki/Dye-sensitized_solar_cell#cite_note-30

[11] C. Simaa, C. Grigoriua, S. Antoheb. Comparison of the dye-sensitized solar cells performances based on transparent conductive ITO and FTO, Thin Solid Films 2010; 519(2): 595-597.

[12] A. Hagfeldt, M. Grätzel. Molecular photovoltaics, Journal of the American Chemical Society 2000; 33(5): 269-277.

[13] B. O'Regan, F. Lenzmann, R. Muis, J. Wienke. A solid-state dye-sensitized solar cell fabricated with pressure-treated P25-TiO_2 and CuSCN: Analysis of pore filling and IV Characteristics, Chemistry of Materials 2002; 14(12): 5023-5029.

[14] T. Taguchi, X.T. Zhang, I. Sutanto, K. Tokuhiro, T.N. Rao, H. Watanabe et al. Improving the performance of solid-state dye-sensitized solar cell using MgO-coated TiO_2 nanoporous film, Chemical Communications 2003; 19: 2480-2481.

[15] K. Murakoshi, R. Kogure, Y. Wada, S. Yanagida, Fabrication of solid-state dye-sensitized TiO2 solar cells combined with polypyrrole, Solar Energy Materials and Solar Cells 1998: 55(1-2): 113-125.

[16] J. Hagen, W. Schaffrath, P. Otschik, et al. Novel hybrid solar cells consisting of inorganic nanoparticles and an organic hole transport material, Synthetic Metals 1997; 89(3): 215–220.

[17] A.C. Arango, L.R. Johnson, V.N. Bliznyuk, Z. Schlesinger, S.A. Carter, H.H. Hörhold. Efficient titanium oxide/conjugated polymer photovoltaics for solar energy conversion, Advanced Materials 2000; 12(22): 1689-1692.

[18] P. Calandra, G. Calogero, A. Sinopoli, P.G. Gucciardi. Metal nanoparticles and carbon-based nanostructures as sdvanced materials for cathode application in dye-sensitized solar cells, International Journal of Photoenergy 2010;

[19] M.K. Nazeeruddin, A. Kay, I. Rodicio, R. Humphry-Baker, E. Mueller, P. Liska et al. Conversion of light to electricity by cis-X2bis(2,2'-bipyridyl-4,4'-dicarboxylate)ruthenium(II) charge-transfer sensitizers (X = Cl-, Br-, I-, CN-, and SCN-) on nanocrystalline titanium dioxide electrodes, Journal of the American Chemical Society 1993; 115(14): 6382-6390.

[20] M.K. Nazeeruddin, P. Péchy, M. Gratzel. Efficient panchromatic sensitization of nanocrystallineTiO2 films by a black dye based on atrithiocyanato–ruthenium complex, Chemical Communications 1997; 1705-1706.

[21] M.K. Nazeeruddin, P. Péchy, T. Renouard, S.M. Zakeeruddin, R. Humphry-Baker, P. Comte et al. Engineering of efficient panchromatic sensitizers for nanocrystalline TiO2-based solar cells, Journal of the American Chemical Society 2001; 123 (8): 1613-1624.

[22] Y. Chiba, A. Islam, Y. Watanabe, R. Komiya, N. Koide, L. Han. Dye-sensitized solar cells with conversion efficiency of 11.1%, Japanese Journal of Applied Physics 2006; 45: L638-L640.

[23] M. Gratzel. Recent advances in sensitized mesoscopic solar cells, Account of Chemical Research 2009; 42(11): 1788-1798.

[24] A. Mishra, M. Fischer, P. Bäuerle. Metal-free organic dyes for dye-sensitized solar cells: from structure: property relationships to design rules. Angewandte Chemie International Edition 2009; 48: 2474-2499.

[25] S. Hwang, J.H. Lee, C. Park, H. Lee, C. Kim, C. Park et al. A highly efficient organic sensitizer for dye-sensitized solar cells, Chemical Communications 2007; 46: 4887-4889.

[26] A. Yella, H.W. Lee, H.N. Tsao, C. Yi, A.K. Chandiran, M.K. Nazeeruddin, E.W. Diau,C.Y. Yeh, S.M. Zakeeruddin, M. Grätzel. A highly efficient organic sensitizer for dye-sensitized solar cells, Chemical Communications 2007; 46: 4887-4889.

[27] H. Zhou, L. Wu, Y. Gao, T. Ma. Dye-sensitized solar cells using 20 natural dyes as sensitizers, Journal of Photochemistry and Photobiology A: Chemistry 2011; 219(2-3): 188-194.

[28] Z. Wang, Y. Cui, Y. Dan-oh, et al. Molecular design of coumarin dyes for stable and efficient organic dye-sensitized solar cells, The Journal of Physical Chemistry C 2008; 112(43): 17011-17017.

[29] N.G. Park, J. van de Lagemaat, A. J. Frank. Comparison of dye-sensitized rutile- and anatase-based TiO_2 solar cells, The Journal of physical Chemistry B 2000; 104(38): 8989-8994.

[30] M. Law, L. Greene, J.C. Johnson, R. Saykkally, P. Yang. Nanowire dye-sensitized solar cells, Nature Materials 2005; 4: 456-459.

[31] G. Redmond, D. Fitzmaurice, M. Gräetzel, Visible light sensitization by cis-Bis (thiocyanato) bis (2,2′- bipyridyl-4, 4′-dicarboxylato)ruthenium(II) of a transparent nanocrystalline ZnO film prepared by sol-gel techniques, Chemistry of Materials 1994; 6(5): 686-691.

[32] K. Keis, E. Magnusson, H. Lindström, S.E Lindquist, A. Hagfeldt. A 5% efficient photoelectrochemical solar cell based on nanostructured ZnO, electrodes Solar Energy Materials and Solar Cells 2002; 73(1): 51-58.

[33] R. Jose, V. Thavasi, S. Ramakrishna. Metal oxides for dye-sensitized solar cells, Journal of the American Ceramic Society 2009; 92(2): 289-301.

[34] M. Saito, S. Fujihara. Large photocurrent in dye-sensitized ZnO solar cells, Energy & Environmental Science 2008; 1: 280-283.

[35] J. Qian, P. Liu, Y. Xiao, Y. Jiang, Y. Cao, X. Ai et al. TiO2-coated multilayered SnO_2 hollow microspheres for dye-sensitized solar cells, Advanced Materials 2009; 21(36): 3663-3667.

[36] C.G. Fonstad, R.H. Rediker. Electrical properties of high quality stannic oxide crystals, Journal of Applied Physics 1971; 42(7): 2911-2918.

[37] R.G. Breckenridge, W.R. Hosler. Electrical properties of titanium dioxide semiconductors, Physics Review 1953; 91(4): 793-802.

[38] E. Ramasamy, J. Lee. Ordered mesoporous SnO_2-based photoanodes for high-performance dye-sensitized solar cells, The Journal of Physical Chemistry C, 2010; 114(50): 22032-22037.

[39] Y. Fukai, Y. Kondo, S.Mori, E. Suzuki. Highly efficient dye-sensitized SnO_2 solar cells having sufficient electron diffusion length, Electrochemistry Communications 2007; 9(7): 1439-1443.

[40] A.N.M. Green, E. Palomares, S.A. Haque, J.M. Kroon, J.R. Durrant. Charge transport versus recombination in dye-sensitized solar cells employing nanocrystalline TiO_2 and SnO_2 films, The Journal of Physical Chemistry B 2005; 109 (25): 12525-12533.

[41] G.A. Parks. The isoelectric points of solid oxides, solid hydroxides, and aqueous hydroxo complex systems, Chemical Reviews 1965; 65(2): 177-198.

[42] M.K.I. Senevirathna, P.K.D.D.P. Pitigala, E.V.A Premalal, K. Tennakone, G.R.A Kumara, A. Konno et al. Stability of the SnO_2/MgO dye-sensitized photoelectrochemical solar cell, Solar Energy Materials and Solar Cells 2007; 91(6): 544-547.

[43] B. Tan, E. Toman, Y. Li, Y. Wu. Zinc stannate (Zn_2SnO_4) dye-sensitized solar cells, Journal of the American Chemical Society 2007; 129(14): 4162-4163.

[44] L. Huang, L. Jianga, M. Wei. Metal-free indoline dye sensitized solar cells based on nanocrystalline Zn_2SnO_4, Electrochemistry Communications 2010; 12(2): 319-322.

[45] M. Ni, M. K. Leung, D. Y. Leung, K. Sumathy. An analytical study of the porosity effect on dye-sensitized solar cell performance, Solar Energy Materials and Solar Cells 2006; 90(9):1331-1344.

[46] K.D. Benkstein, N. Kopidakis, J. van de Lagemaat, A.J. Frank. Influence of the percolation network geometry on electron transport in dye-sensitized titanium dioxide solar cells, The Journal of Physical Chemistry B 2003; 107(31): 7759-7767.

[47] M. Grätzel. Dye-sensitized solar cells, Journal of Photochemistry and Photobiology C: Photochemistry Reviews 2003; 4(2): 145-153.

[48] S. Sato, S. Oimatsu, R. Takahashi. Pore size regulation of TiO_2 by use of a complex of titanium tetraisopropoxide and stearic acid, Chemical Communications 1997; 2219-2220.

[49] C.J. Barbé, F. Arendse, P. Comte, M. Jirousek, F. Lenzmann, V. Shklover et al. Nanocrystalline titanium oxide electrodes for photovoltaic applications, Journal of the American Ceramic Society 1997; 80(12): 3157-3171.

[50] Y, Saito, S. Kambe, T. Kitamura, Y. Wada, S. Yanagida. Morphology control of mesoporous TiO_2 nanocrystalline films for performance of dye-sensitized solar cells, Solar Energy Materials and Solar Cells 2004; 3(1): 1-13.

[51] Z. Wang, H. Kawauchi, T. Kashima, H. Arakawa. Significant influence of TiO_2 photoelectrode morphology on the energy conversion efficiency of N719 dye-sensitized solar cell, Coordination Chemistry Reviews 2004; 248(13-14): 1381-1389.

[52] A. Solbrand, H. Lindström, H. Rensmo, A. Hagfeldt, S.E Lindaquist. Electron transport in the nanostructured TiO_2-electrolyte system studied with time-resolved photocurrents, The Journal of Physical Chemistry B 1997; 101(14): 2514-2518.

[53] A.C. Fisher, L.M. Peter, E.A. Ponomarev, A.B. Walker, K.G.U. Wijayantha. Intensity dependence of the back reaction and transport of electrons in dye-sensitized nanocrystalline TiO_2 solar cells, The Journal of Physical Chemistry B 2000; 104(5): 949-958.

[54] M. Adachi, Y. Murata, J. Takao, J. Jiu, M. Sakamoto, F. Wang. Highly efficient dye-sensitized solar cells with a titania thin-film electrode composed of a network structure of single-crystal-like TiO_2 nanowires made by the "Oriented Attachment" mechanism, Journal of the American Chemical Society 2004; 126(45): 14943-14949.

[55] A.J. Frank, N. Kopidakis, J. van de Lagemaat, Electrons in nanostructured TiO_2 solar cells: transport, recombination and photovoltaic properties, Coordination Chemistry Reviews 2004; 248(13-14): 1165-1179.

[56] L.E. Greene, M. Law, J. Goldberger, F. Kim, J.C. Johnson, Y. Zhang. Low-temperature wafer scale production of ZnO nanowire arrays, Angewandte Chemie International Edition 2003; 42(26): 3031-3034.

[57] M. Adachi, Y. Murata, I. Okada, S. Yoshikawa. Formation of titania nanotubes and applications for dye-sensitized solar cells, Journal of The Electrochemical Society 2003; 150(8): G488-G493.

[58] K. Shankar, J.I. Basham, N.K. Allam, O.K.Varghese, G.K Mor, X. Feng et al. Recent advances in the use of TiO_2 nanotube and nanowire arrays for oxidative photoelectrochemistry, The Journal of Physical Chemistry C 2009; 113(16): 6327-6359.

[59] K. Shankar, G.K. Mor, H.E. Prakasam, S. Yoriya, M. Paulose, O.K. Varghese et al. Highly-ordered TiO_2 nanotube arrays up to 220 μm in length: use in water hotoelectrolysis and dye-sensitized solar cells, Nanotechnology 2007; 18(6): 065707.

[60] B.X. Lei, J.Y. Liao, R. Zhang, J. Wang, C.Y. Su, D.B. Kuang. Ordered crystalline TiO_2 nanotube arrays on transparent FTO glass for efficient dye-sensitized solar cells, The Journal of Physical Chemistry C 2010; 114(35): 15228-15233.

[61] D. Chen, F. Huang, Y. Cheng, R.A. Caruso. Mesoporous anatase TiO_2 beads with high surface areas and controllable pore sizes: a superior candidate for high-performance dye-Sensitized Solar Cells, Advanced Materials 2009; 21(21): 2206-2210.

[62] S.C. Yang, D.J. Yang, J. Kim. Hollow TiO_2 hemispheres obtained by colloidal templating for application in dye-sensitized solar cells, Advanced Materials 2008; 20(5): 1059-1064.

[63] G. Boschloo, A. Hagfeldt. Characteristics of the iodide/triiodide redox mediator in dye-sensitized solar cells, Accounts of Chemical Research 2009; 42(11): 1819-1826.

[64] J. Qian, P. Liu, Y. Xiao, Y. Jiang, Y. Cao, X. ai et al. TiO2-coated multilayered SnO_2 hollow microspheres for dye-sensitized solar cells, Advanced Materials 2009; 21(36): 3663-3667.

[65] M.T. Zanni, B.J. Greenblatt, A.V. Davis, D.M. Neumark. Photodissociation of gas phase I3− using femtosecond photoelectron spectroscopy, The Journal of Chemical Physics 1999; 111(7): 2991-3003.

[66] G. Boschloo, L. Häggman, A. Hagfeldt. Quantification of the effect of 4-tert-butylpyridine addition to I^-/I_3^- redox electrolytes in dye-sensitized nanostructured TiO_2 solar cells. The Journal of Physical Chemistry B 2006; 110(26): 13144-13150.

[67] N. Kopidakis, N.R. Neale, A.J. Frank. Effect of an adsorbent on recombination and band-edge movement in dye-sensitized TiO_2 solar cells: evidence for surface passivation. The Journal of Physical Chemistry B 2006; 110(25), 12485-12489.

[68] E. Figgemeier, A. Hagfeldt, Are dye-sensitized nano-structured solar cells stable? An overview of device testing and component analyses, International Journal of Photoenergy 2004; 6: 127-140.

[69] Z. Zhang, N. Evans, S.M. Zakeeruddin, R. Humphry-Baker, M. Grätzel. Effects of ω-guanidinoalkyl acids as coadsorbents in dye-sensitized solar cells. The Journal of Physical Chemistry C 2007; 111(1): 398-403.

[70] M. Wang, N. Chamberland, L. Breau, J.E. Moser, R. Humphry-Baker, B. Marsan et al. An organic redox electrolyte to rival triiodide/iodide in dye-sensitized solar cells, Nature Chemistry 2010; 2: 385-389.

[71] S.M. Feldt, E.A. Gibson, E. Gabrielsson, L. Sun, G. Boschloo, A. Hagfeldt. Design of organic dyes and cobalt polypyridine redox mediators for high-efficiency dye-sensitized solar cells, Journal of the American Chemical Society 2010; 132(46): 16714-16724.

[72] S.M. Zakeeruddin, M. Grätzel. Solvent-free ionic liquid electrolytes for mesoscopic dye-sensitized solar cells, Advanced Functional Materials 2009; 19(14): 2187-2202.

[73] L.M. Gonçalves, V. de Z. Bermudez, H.A. Ribeiro, A.M. Mendes. Dye-sensitized solar cells: A safe bet for the future, Energy & Environmental Science 2008; 1(6): 655-667.

[74] N. Papageorgiou, Y. Athanassov, M. Armand, P. Bonhôte, H. Pettersson, A. Azam et al. The performance and stability of ambient temperature molten salts for solar cells application, Journal of The Electrochemical Society 1996; 143(10): 3099-3108.

[75] M. Gorlov, H. Pettersson, A. Hagfeldt, L. Kloo. Electrolytes for dye-sensitized solar cells based on interhalogen ionic salts and liquids, Inorganic Chemistry 2007; 46(9): 3566-3575.

[76] Y. Bai, Y. Cao, J. Zhang, M. Wang, R. Li, P. Wang et al. High-performance dye-sensitized solar cells based on solvent-free electrolytes produced from eutectic melts, Nature Materials 2008; 7: 626-630.

[77] K. Tennakone, G.R.R.A Kumara, A.R. Kumarasinghe, K.G.U. Wijayantha, P.M. Sirimanne . A dye-sensitized nano-porous solid-state photovoltaic cell, Semiconductor Science and Technology 1995; 10(12): 1689-1693.

[78] B. O'Regan, D.T Schwartz. Efficient photo-hole injection from adsorbed cyanine dyes into electrodeposited copper(I) thiocyanate thin films, Chemistry of Materials 1995; 7(7): 1349-1354.

[79] G.R.A. Kumara, S. Kaneko, M. Okuya, K. Tennakone. Fabrication of dye-sensitized solar cells using triethylamine hydrothiocyanate as a CuI crystal growth inhibitor, Langmuir 2002; 18(26): 10493-10495.

[80] L. Heng, X. Wang, N. Yang, J. Zhai, M. Wan, L. Jiang. P-n-junction-based flexible dye-sensitized solar cells, Advanced Functional Materials 2010; 20(2): 266-271.

[81] U. Bach, D. Lupo, P. Comte, J.E. Moser, F. Weissörtel, J. Salbeck et al. Solid-state dye-sensitized mesoporous TiO_2 solar cells with high photon-to-electron conversion efficiencies, Nature 1998; 395: 583-585.

[82] G. Kron, T. Egerter, J.H. Werner, U. Ran. Electronic transport in dye-sensitized nanoporous TiO2 solar cells-comparison of electrolyte and solid-state devices, The Journal of Physical Chemistry 2003; 107(15): 3556-3564.

[83] P. Wang, S.M. Zakeeruddin, J.E. Moser, M.K. Nazeeruddin, T. Sekiguchi, M. Grätzel. A stable quasi-solid-state dye-sensitized solar cell with an amphiphilic ruthenium sensitizer and polymer gel electrolyte, Nature Materials 2003; 2(6): 402-407.

[84] P. Wang, S.M. Zakeeruddin, P. Comte, I. Exnar, M. Gräztel. Gelation of ionic liquid-based electrolytes with silica nanoparticles for quasi-solid-state dye-sensitized solar cells, Journal of the American Chemical Society 2003; 125(5): 1166-1167.

[85] R.B.H. Tahar, T. Ban, Y. Ohya, Y. Takahashi. Tin doped indium oxide thin films: electrical properties, Journal of Applied Physics 1998; 83(5): 2631-2645.

[86] I. Hamberg, C.G. Granqvist. Evaporated Sn‐doped In2O3 films: Basic optical properties and applications to energy‐efficient windows, Journal of Applied Physics 1986; 60(11): R123-R159.

[87] S. Ngamsinlapasathian, T. Sreethawong, Y. Suzuki, S. Yoshikawa. Doubled layered ITO/SnO_2 conducting glass for substrate of dye-sensitized solar cells, Solar Energy Materials and Solar Cells 2006; 90(14): 2129-2140.

[88] S. Ngamsinlapasathian,T. Sreethawong, S. Yoshikawa. Enhanced efficiency of dye-sensitized solar cell using double-layered conducting glass, Thin Solid Films 2008; 516(21): 7802-7806.

[89] F. Yang, Thin film solar cells grown by organic vapor phase deposition, Doctor thesis 2008, Princeton University.

[90] C. Sima, C. Grigoriu, S. Antohe. Comparison of the dye-sensitized solar cells performances based on transparent conductive ITO and FTO, Thin Solid Films 2010; 519(2):595-597.

[91] Z. Chen, B. Cotterell, W. Wang, E. Guenther, S.J. Chua. A mechanical assessment of flexible optoelectronic devices, Thin Solid Films 2001; 394(1-2): 201-205.

[92] X. Wang, L. Zhi, K. Mullen. Transparent, conductive graphene electrodes for dye-sensitized solar cells, Nano Letters 2008; 8(1): 323-327.

[93] H. Zhu, J. Wei, K. Wang, D. Wu. Applications of carbon materials in photovoltaic solar cells, Solar Energy Materials & Solar Cells 2009; 93: 1461-1470.

[94] B. Sharma, Metal-semiconductor Schottky barrier junctions and their application, Plenum Pub Corp, 1984.

[95] A. Bard and L. Faulkner, Electrochemical methods, fundamentals and applications, Wiley, John & Sons, 2001.

[96] Hauch, A. Georg. Diffusion in the electrolyte and charge-transfer reaction at the platinum electrode in dye-sensitized solar cells, Electrochimica Acta 2001; 46: 3457-3466.

[97] Z. Lan, J. Wu, D. Wang, S. Hao, J. Lin, Y. Huang. Quasi-solid dye-sensitized solar cells based on a sol-gel organic-inorganic composite electrolyte containing an organic iodide salt, Solar Energy 2007; 81: 117-122.

[98] L. Han, N. Koide, Y. Chiba, T. Mitate. Modeling of an equivalent circuit for dye-sensitized solar cells, Applied Physics Letters 2004; 84(13): 2433-2435.

[99] Q. Wang, J.E. Moser, M. Gratzel. Electrochemical impedance spectroscopic analysis of dye-sensitized solar cells 2005; 109: 14945-14953.

[100] http://www.rssweather.com/climat/North%20Dakota/Fargo/

[101] S. Sodergren, A. Hagfeldt, J. Olsson, S.E. Lindquist. Theoretical models for the action spectrum and the current-voltage characteristics of microporous semiconductor films in photoelectrochemical cells, The Journal of Physical Chemistry 1994; 98(21): 5552-5556.

[102] G. Kron, U. Rau, J.H. Werner. Influence of the built-in voltage on the fill factor of dye-sensitized solar cells, The Journal of Physical Chemistry B 2003; 107: 13258-13261.

[103] J. Ferber, R. Stangl, J. Luther. An electrical model of the dye-sensitized solar cell, Solar Energy Materials and Solar Cells 1998; 53(1-2): 29-54.

[104] J.J. Lee, G.M. Coia, N.S. Lewis. Current density versus potential characteristics of dye-sensitized nanostructured semiconductor photoelectrodes. 2. Simulations, The Journal of Physical Chemistry B 2004; 108(17): 5269-5281.

[105] M. Ni, M.K.H. Leung, D.Y.C. Leung, K. Sumathy. Theoretical modeling of TiO_2/TCO interfacial effect on dye-sensitized solar cell performance, Solar Energy Materials and Solar Cells 2006; 90(13): 2000-2009.

[106] G. Rothenberger, D. Fitzmaurice, M. Graetzel. Spectroscopy of conduction band electrons in transparent metal oxide semiconductor films: optical determination of the flatband potential of colloidal titanium dioxide films, The Journal of Physical Chemistry 1992; 96(14): 5983-5986.

[107] J. Ferber, J. Luther. Modeling of photovoltage and photocurrent in dye-sensitized titanium dioxide solar cells, The Journal of Physical Chemistry B 2001; 105(21): 4895-4903.

[108] F. Cao, G. Oskam, G.J. Meyer, P.C. Searson. Electron transport in porous nanocrystalline TiO_2 photoelectrochemical cells, The Journal of Physical Chemistry 1996; 100(42): 17021-17027.

[109] M. Penny, T. Farrell, G. Will. A mathematical model for the anodic half cell of a dye-sensitised solar cell, Solar Energy Materials and Solar Cells 2008; 92(1): 24-37.

[110] N. Papageorgiou, M. Grätzel, P.P. Infelta. On the relevance of mass transport in thin layer nanocrystalline photoelectrochemical solar cells, Solar Energy Materials and Solar Cells 1996; 44(4): 405-438.

[111] W.H. Press, B.P. Flannery, S.A.Teukolsky , W.T. Vetterling , 1992. Numerical Recipes in C: The Art of Scientific Computing, Cambridge University Press.

[112] M. Berginc, U.O. Krasovec, M. Jankovec, M. Topic. The effect of temperature on the performance of dye-sensitized solar cells based on a propyl-methyl-imidazolium iodide electrolyte, Solar Energy Materials and Solar Cells 2007; 91(9): 821-828.

[113] P.J. Cameron, L. M. Peter. How does back-reaction at the conducting glass substrate influence the dynamic photovoltage response of nanocrystalline dye-sensitized solar cells, The Journal of Physical Chemistry B 2005; 109(15): 7392-7398.

[114] A. Tricoli, A.S. Wallerand, and M. Righettoni. Highly porous TiO_2 films for dye sensitized solar cells. Journal of Materials Chemistry 2012; 22, 14254-14261.

[115] L.Y. Han, N. Koide, Y. Chiba, A. Islam, R. Koiya, N Fuke, A. Fukui, R. Yamanaka. Improvement of efficiency of dye-sensitized solar cells by reduction of internal resistance. Applied Physics Letter 2005; 86(21), 213501.

[116] Y. Huang, S.Y. Dai, S.D. Chen, C.N. Zhang, Y.F. Sui, S.F. Xiao, L.H. Hu. Theoretical modeling of the series resistance effect on dye-sensitized solar cell performance. Applied Physics Letter 2009; 95, 24503.

[117] A. Zaban, A. Meier, B.A. Gregg. Electric potential distribution and short-range screening in nanoporous TiO_2 electrodes. Journal of Physical Chemistry 1997; 101(40), 7985-7990.

[118] A. Usami "Analysis of energy conversion efficiency with an empirical model in dye-sensitized nanocrystalline solar cells," Electrochemical and Solid State Letters 2003; 6, A236-A239.

[119] J.W. Gong, J. Liang, K. Sumathy. Review on dye-sensitized solar cells (DSCs): Fundamental concepts and novel materials, Renewable & Sustainable Energy Reviews 2012; 16, 5848-5860.

[120] B.O. Aduda, P. Ravirajan, K.L. Choy, J. Nelson. Effect of morphology on electron drift mobility in porous TiO_2. International Journal of Photoenergy 2004; 6(3), 141-147.

[121] S. Tanaka, Performance simulation for dye-sensitized solar cells: Towards high efficiency and solid state. Japanese Journal of Applied Physics Part I-Regular Papers Short Notes & Review Papers 2001; 40, 97-107.

[122] M.G. Kang, K.S. Ryu, S.H. Chang, N.G. Park, J.S. Hong, K.J. Kim. Dependence of TiO_2 film thickness on photocurrent-voltage characteristics of dye-sensitized solar cells. Bulletin of the Korean Chemical Society 2004; 25, 742-744.

[123] X.M. Fang, T.L. Ma, G.Q. Guan, M. Akiyama, T. Kida, E. Abe. Effect of the thickness of the Pt film coated on a counter electrode on the performance of a dye-sensitized solar cell. Journal of Electroanalytical Chemistry 2004; 570, 257-263.

APPENDIX A. NUMERICAL ASPECTS

In relaxation methods we replace ODEs by approximate finite-difference equations (FDEs) on a grid or mesh of points that spans the domain of interest.

As a typical example, we could replace a general first-order differential equation

$$\frac{dy}{dx} = g(x, y) \tag{A.1}$$

with an algebraic equation relating function values at two points k, $k-1$:

$$y_k - y_{k-1} - (x_k - x_{k-1}) g\left[\frac{1}{2}(x_k + x_{k-1}), \frac{1}{2}(y_k + y_{k-1})\right] = 0 \tag{A.2}$$

When the problem involves N coupled first-order ODEs represented by FDEs on a mesh of M points, a solution consists of values for N dependent functions given at each of the M mesh points, or $N \times M$ variables in all. The relaxation method determines the solution by starting with a guess and improving it, iteratively. As the iterations improve the solution, the results is said to relax to the true solution.

We use the notation $\boldsymbol{y}_k$ to refer to the entire set of dependent variables $y_1, y_2, \ldots, y_N$ at point x_k. At an arbitrary point k in the middle of the mesh, we approximate the set of N first-order ODEs by algebraic relations of the form

$$0 = \boldsymbol{E}_k \equiv \boldsymbol{y}_k - \boldsymbol{y}_{k-1} - (x_k - x_{k-1}) \boldsymbol{g}_k(x_k, x_{k-1}, \boldsymbol{y}_k, \boldsymbol{y}_{k-1}), k = 2,3, \ldots, M \tag{A.3}$$

Thus the FDEs provide a total of $(M-1)N$ equations for the MN unknowns. The remaining N equations come from the boundary conditions.

At the first boundary we have

$$0 = \boldsymbol{E}_1 \equiv \boldsymbol{B}(x_1, \boldsymbol{y}_1) \tag{A.4}$$

While at the second boundary

$$0 = \boldsymbol{E}_{M+1} \equiv \boldsymbol{C}(x_M, \boldsymbol{y}_M) \tag{A.5}$$

Equations for the increments are developed by expanding the FDEs in first-order Taylor series with respect to small changes $\Delta\mathbf{y}_k$. At an interior point, $k = 2,3,\dots,M$ this gives:

$$\mathbf{E}_k(\mathbf{y}_k + \Delta\mathbf{y}_k, \mathbf{y}_{k-1} + \Delta\mathbf{y}_{k-1}) \approx \mathbf{E}_k(\mathbf{y}_k, \mathbf{y}_{k-1}) + \sum_{n=1}^{N} \frac{\partial \mathbf{E}_k}{\partial y_{n,k-1}} \Delta y_{n,k-1} + \sum_{n=1}^{N} \frac{\partial \mathbf{E}_k}{\partial y_{n,k}} \Delta y_{n,k} \tag{A.6}$$

For a solution we want the updated value $\mathbf{E}(\mathbf{y} + \Delta\mathbf{y})$ to be zero, so the general set of equations at an interior point can be written in matrix form as

$$\sum_{n=1}^{N} S_{j,n} \Delta y_{n,k-1} + \sum_{n=N+1}^{2N} S_{j,n} \Delta y_{n-N,k} = -E_{j,k}, \qquad j = 1,2,\dots,N \tag{A.7}$$

Where

$$S_{j,n} = \frac{\partial E_{j,k}}{\partial y_{n,k-1}}, \qquad S_{j,n+N} = \frac{\partial E_{j,k}}{\partial y_{n,k}}, \qquad n = 1,2,\dots,N \tag{A.8}$$

APPENDIX B. PROGRAM CODE

B.1. Global System Model

```
 %%%%  Main program
clc;
clear all;

jg = 0;                                     %% initial current density value
h = 5;                                      %% current density increment

Volt = Simcase(jg);
jext = jg;
error = 1;                                  %% pre-defined error
iter = 0;                                   %% Number of iteration

while Volt >= 0;
    iter = iter + 1;
    jg = jg + h;
    V = Simcase(jg);
    if isreal(V)
        jext = [jext,jg];
        Volt = [Volt,V];
    else jg = jg - h;
        h = h/10;
    end
end
    Volt(end) = 0;



clc;
fprintf('J-V: %4.2f mA, %10.4f V\n',[jext; Volt]);

x = min(Volt):0.01:max(Volt);
y = pchip(Volt,jext,x);
indices = find(x.*y == max(x.*y) );
maxpoint = [x(indices),y(indices)];
maxpw = x(indices)*y(indices);
jv = [x',y'];

ff = maxpw/(max(x)*max(y));    % Fill factor

plot(Volt,jext,'d')
hold on
plot(x,y)
```

B.2. ODE Solver

```
function [Volt] = Simcase(jg)

M = 150;
p = linspace(1,M,M);
chi = 1/2*cos(pi/(M-1) * (p+M-2)) + 1/2;
N = 9;                                                  %% nine variales

%%        Material parameters, intl system, if not mentioned.
e0 = 1.6*10^-19;
ke = 10^4;
h = 6.626 * 10^-34;
k = 1.38 * 10^-23;
epsilon = 50;
epsilon0 = 8.854*10^-12;
d = 10*10^-6;
me = 9.109*10^-31;
mes = 5.6*me;
T = 298; % Temperature
NCB = 2*((2*pi*mes*k*T)/(h^2))^1.5; % NCB
nedr = 2.3*10^10; % ne under dark


%%         Mobility & Diffusion constant in TiO2 nanopaticle
mue =  0.3 * 10^-4;
Dr  =  8.5 * 10^-10;
Do  =  8.5 * 10^-10;
De  =  mue * k * T / e0;

As  = 6.71*10^6;  % Richardson constant of TiO2, unit Am^-2K^-2
Phi = 0.5;     % Schottky Barrier, unit eV

%%         Initial concentration
por = 0.5;       %posoristy
Cri = 0.45;    %unit M=mol/L
Coi = 0.05;    %unit M
nri = 2.71 * 10^26 * por;
noi = 3.01 * 10^25 * por;
nei = nedr;
nci = nri + noi + nei;

% typical scale value
Jt = 10;              %unit A/m^2
nt = 10^23;           %unit m^-3
Et = 10^3;            %unit v/m


%% initial guess
Y = zeros(N,M);     % claim a space of all variables (first index refer to
variable, second refer to points)
Y(1,:) = linspace(jg/Jt,0,M);
Y(2,:) = 0.02;
Y(3,:) = nri/nt;
```

```
Y(4,:) = noi/nt;
Y(5,:) = nci/nt;
Y(6,:) = 0;
Y(7,:) = linspace(0,nci/nt,M);
Y(8,:) = linspace(0,(noi+1/3*nri)/nt,M);
Y(9,:) = linspace(0,(1/2*nei+1/3*nri)/nt,M);

%% Asemble matrix
s = zeros(N,2*N);   %% N = Number of variables
X(N,2*N,M+1) = 0;

for i = 2:M         %% M = Number of mesh points, and every iteration produce
one block of matrix except boundary conditions

s(1,1) = -1;
s(1,2) = -(chi(i) - chi(i-1))*(d*e0*ke*nt/2/Jt)*((Y(4,i)+Y(4,i-
1))/(Y(3,i)+Y(3,i-1)))^.5;
s(1,3) = (chi(i)-chi(i-1))*(d*e0*ke*nt/2/Jt)*((Y(2,i)+Y(2,i-
1))/2/(Y(3,i)+Y(3,i-1))*((Y(4,i)+Y(4,i-1))/(Y(3,i)+Y(3,i-1)))^.5 +
(noi/nri)^0.5*nei/nri);
s(1,4) = -(chi(i)-chi(i-1))*(d*e0*ke*nt/2/Jt)*(Y(2,i)+Y(2,i-
1))/2/((Y(3,i)+Y(3,i-1))*(Y(4,i)+Y(4,i-1)))^0.5;
s(1,5:9) = 0;
s(1,10) = 1;
s(1,11:18) = s(1,2:9);

s(2,1) = -(chi(i) - chi(i-1))*(d*Jt/(2*e0*nt*De));
s(2,2) = -1 + (chi(i) - chi(i-1))*(d*e0*Et/(4*k*T))*(Y(6,i)+Y(6,i-1));
s(2,3:5) = 0;
s(2,6) = (chi(i) - chi(i-1))*(d*e0*Et/(4*k*T))*(Y(2,i)+Y(2,i-1));
s(2,7:9) = 0;
s(2,10:18) = s(2,1:9);
s(2,11) = 1 + (chi(i) - chi(i-1))*(d*e0*Et/(4*k*T))*(Y(6,i)+Y(6,i-1));

s(3,1) = (chi(i) - chi(i-1))*(3*d*Jt/(4*e0*nt*Dr));
s(3,2) = 0;
s(3,3) = -1 + (chi(i) - chi(i-1))*(d*e0*Et/(4*k*T))*(Y(6,i)+Y(6,i-1));
s(3,4:5) = 0;
s(3,6) = (chi(i) - chi(i-1))*(d*e0*Et/(4*k*T))*(Y(3,i)+Y(3,i-1));
s(3,7:9) = 0;
s(3,10:18) = s(3,1:9);
s(3,12) = 1 + (chi(i) - chi(i-1))*(d*e0*Et/(4*k*T))*(Y(6,i)+Y(6,i-1));

s(4,1) = -(chi(i) - chi(i-1))*(d*Jt/(4*e0*nt*Do));
s(4,2:3) = 0;
s(4,4) = -1 + (chi(i) - chi(i-1))*(d*e0*Et/(4*k*T))*(Y(6,i)+Y(6,i-1));
s(4,5) = 0;
s(4,6) = (chi(i) - chi(i-1))*(d*e0*Et/(4*k*T))*(Y(4,i)+Y(4,i-1));
s(4,7:9) = 0;
s(4,10:18) = s(4,1:9);
s(4,13) = 1+ (chi(i) - chi(i-1))*(d*e0*Et/(4*k*T))*(Y(6,i)+Y(6,i-1));

s(5,1:18) = 0;
s(5,5) = -1 - (chi(i) - chi(i-1))*(d*e0*Et/(4*k*T))*(Y(6,i)+Y(6,i-1));
s(5,14) = 1 - (chi(i) - chi(i-1))*(d*e0*Et/(4*k*T))*(Y(6,i)+Y(6,i-1));
```

```
s(5,6) = -(chi(i) - chi(i-1))*(d*e0*Et/(4*k*T))*(Y(5,i)+Y(5,i-1));
s(5,15) = s(5,6);

s(6,1) = 0;
s(6,2) = (chi(i) - chi(i-1))*(d*e0*nt/(2*Et*epsilon*epsilon0));
s(6,3:4) = s(6,2);
s(6,5) = -s(6,2);
s(6,6) = -1;
s(6,7:9) = 0;
s(6,10:18) = s(6,1:9);
s(6,15) = 1;

s(7,1:18) = 0;
s(7,5) = -1/2*(chi(i) - chi(i-1));
s(7,7) = -1;
s(7,14) = s(7,5);
s(7,16) = 1;

s(8,1:18) = 0;
s(8,3) = -1/6*(chi(i) - chi(i-1));
s(8,4) = -1/2*(chi(i) - chi(i-1));
s(8,8) = -1;
s(8,12:13) = s(8,3:4);
s(8,17) = 1;

s(9,1:18) = 0;
s(9,2) = -1/4*(chi(i) - chi(i-1));
s(9,3) = -1/6*(chi(i) - chi(i-1));
s(9,9) = -1;
s(9,11:12) = s(9,2:3);
s(9,18) = 1;

X(:,:,i) = s;

end

%% boundary conditions
n1 = 5;                          % n1 = Number of boundary conditions at x = 0
n2 = 4;                          % n2 = Number of boundary conditions at x = d

% First boundary conditions at x=0
X1= zeros(5,9);                  % matrix X1
X1(1,1) = 1;
X1(2,6) = 1;
X1(3,7) = 1;
X1(4,8) = 1;
X1(5,9) = 1;

% Second boundary conditions at x=d

XM = zeros(4,9);          %% matrix X(M+1)
XM(1,1) = 1;
XM(2,7) = 1;
XM(3,8) = 1;
XM(4,9) = 1;
```

```
%% Assemble Coefficient matrix coeff

coeff = zeros(N*M);

coeff(1:n1,1:N) = X1;                          % first boudary conditions

for i = 0:M-2
    coeff(n1+i*N+1:n1+(i+1)*N, i*N+1:(i+2)*N) = X(:,:,i+2);
end

coeff(N*M-3:N*M,N*M-8:N*M) = XM;                % second boudary conditions


%% known right-hand side

E = zeros(N,M+1);

Ge = Gen(chi,d);

for j = 2:M

E(1,j) = (Y(1,j)-Y(1,j-1)) - (chi(j) - chi(j-1)) * ...
    (d*e0*ke/(2*Jt) * (nt*(Y(2,j)+Y(2,j-1))*((Y(4,j)+Y(4,j-1))/(Y(3,j)+Y(3,j-
1)))^0.5 - nei*nt*(Y(3,j)+Y(3,j-1))*(noi/nri^3)^0.5) - d*e0/Jt*Ge(j));

E(2,j) = (Y(2,j)-Y(2,j-1)) - (chi(j) - chi(j-1)) *...
    (d*Jt/(2*e0*nt*De)*(Y(1,j)+Y(1,j-1))-(d*e0*Et/(4*k*T))*(Y(2,j)+Y(2,j-
1))*(Y(6,j)+Y(6,j-1)));

E(3,j) = (Y(3,j)-Y(3,j-1)) - (chi(j) - chi(j-1)) *...
    (3*d/(2*e0*nt*Dr)*(jg - Jt*(Y(1,j)+Y(1,j-1))/2) -
(d*e0*Et/(4*k*T))*(Y(3,j)+Y(3,j-1))*(Y(6,j)+Y(6,j-1)));

E(4,j) = (Y(4,j)-Y(4,j-1)) - (chi(j) - chi(j-1)) *...
    (-d/(2*e0*nt*Do)*(jg - Jt*(Y(1,j)+Y(1,j-1))/2)-
(d*e0*Et/(4*k*T))*(Y(4,j)+Y(4,j-1))*(Y(6,j)+Y(6,j-1)));

E(5,j) = (Y(5,j)-Y(5,j-1)) - (chi(j) - chi(j-1)) *...
    (d*e0*Et/(4*k*T)) * (Y(5,j)+Y(5,j-1)) * (Y(6,j)+Y(6,j-1));

E(6,j) = (Y(6,j)-Y(6,j-1)) - (chi(j) - chi(j-1)) *...
    (d*e0*nt/(2*Et*epsilon*epsilon0)) * ( (Y(5,j)+Y(5,j-1)) - (Y(2,j)+Y(2,j-
1)) - (Y(3,j)+Y(3,j-1)) - (Y(4,j)+Y(4,j-1)) );

E(7,j) = (Y(7,j)-Y(7,j-1)) - (chi(j) - chi(j-1)) * ( 1/2*(Y(5,j)+Y(5,j-1)) );

E(8,j) = (Y(8,j)-Y(8,j-1)) - (chi(j) - chi(j-1)) * ( 1/2*(Y(4,j)+Y(4,j-1)) +
1/6*(Y(3,j)+Y(3,j-1)) );

E(9,j) = (Y(9,j)-Y(9,j-1)) - (chi(j) - chi(j-1)) * ( 1/4*(Y(2,j)+Y(2,j-1)) +
1/6*(Y(3,j)+Y(3,j-1)) );
```

```
end

% At first boundaries

E(n2+1:9,1) = [Y(1,1)-jg/Jt; Y(6,1); Y(7,1); Y(8,1); Y(9,1)];

% At second boundaries

E(1:n2,M+1) = [Y(1,M); Y(7,M)-nci/nt; Y(8,M)-(noi+1/3*nri)/nt; Y(9,M)-
(1/2*nei+1/3*nri)/nt];

% Assemble known right-hand side

B = zeros(M*N,1);

B(1:n1) = E(n2+1:9,1);                              % At first boundaries

B(M*N-n2+1:M*N) = E(1:n2,M+1);                      % At second boundaries

for i=0:M-2
    B(n1+1+i*N:n1+(i+1)*N) = E(1:N, 2+i);
end

B = -B;


%% unkown solution vector, to compare different method

C = [coeff,B];                    % C is augmented matrix, used to scale
for ij = 1:M*N
    C(ij,:) = C(ij,:)/abs(max(C(ij,:)));
end

V = pinv(C(1:M*N,1:M*N))*C(1:M*N,1+M*N);

%% update Y(:,:) matrix by adding incrument V

for ii = 1:M
    Y(:,ii) = Y(:,ii) + V(1+(ii-1)*N:ii*N);
end


%% interation

count = 1;
tol = 10^-5;
while norm(V)>tol

%% Asemble matrix
```

```
for i = 2:M          % M = Number of mesh points, and every iteration produce
one block of matrix except boundary conditions

s(1,1) = -1;
s(1,2) = -(chi(i) - chi(i-1))*(d*e0*ke*nt/2/Jt)*((Y(4,i)+Y(4,i-
1))/(Y(3,i)+Y(3,i-1)))^.5;
s(1,3) = (chi(i)-chi(i-1))*(d*e0*ke*nt/2/Jt)*((Y(2,i)+Y(2,i-
1))/2/(Y(3,i)+Y(3,i-1))*((Y(4,i)+Y(4,i-1))/(Y(3,i)+Y(3,i-1)))^.5 +
(noi/nri)^0.5*nei/nri);
s(1,4) = -(chi(i)-chi(i-1))*(d*e0*ke*nt/2/Jt)*(Y(2,i)+Y(2,i-
1))/2/((Y(3,i)+Y(3,i-1))*(Y(4,i)+Y(4,i-1)))^0.5;
s(1,5:9) = 0;
s(1,10) = 1;
s(1,11:18) = s(1,2:9);

s(2,1) = -(chi(i) - chi(i-1))*(d*Jt/(2*e0*nt*De));
s(2,2) = -1 + (chi(i) - chi(i-1))*(d*e0*Et/(4*k*T))*(Y(6,i)+Y(6,i-1));
s(2,3:5) = 0;
s(2,6) = (chi(i) - chi(i-1))*(d*e0*Et/(4*k*T))*(Y(2,i)+Y(2,i-1));
s(2,7:9) = 0;
s(2,10:18) = s(2,1:9);
s(2,11) = 1 + (chi(i) - chi(i-1))*(d*e0*Et/(4*k*T))*(Y(6,i)+Y(6,i-1));

s(3,1) = (chi(i) - chi(i-1))*(3*d*Jt/(4*e0*nt*Dr));
s(3,2) = 0;
s(3,3) = -1 + (chi(i) - chi(i-1))*(d*e0*Et/(4*k*T))*(Y(6,i)+Y(6,i-1));
s(3,4:5) = 0;
s(3,6) = (chi(i) - chi(i-1))*(d*e0*Et/(4*k*T))*(Y(3,i)+Y(3,i-1));
s(3,7:9) = 0;
s(3,10:18) = s(3,1:9);
s(3,12) = 1 + (chi(i) - chi(i-1))*(d*e0*Et/(4*k*T))*(Y(6,i)+Y(6,i-1));

s(4,1) = -(chi(i) - chi(i-1))*(d*Jt/(4*e0*nt*Do));
s(4,2:3) = 0;
s(4,4) = -1 + (chi(i) - chi(i-1))*(d*e0*Et/(4*k*T))*(Y(6,i)+Y(6,i-1));
s(4,5) = 0;
s(4,6) = (chi(i) - chi(i-1))*(d*e0*Et/(4*k*T))*(Y(4,i)+Y(4,i-1));
s(4,7:9) = 0;
s(4,10:18) = s(4,1:9);
s(4,13) = 1+ (chi(i) - chi(i-1))*(d*e0*Et/(4*k*T))*(Y(6,i)+Y(6,i-1));

s(5,1:18) = 0;
s(5,5) = -1 - (chi(i) - chi(i-1))*(d*e0*Et/(4*k*T))*(Y(6,i)+Y(6,i-1));
s(5,14) = 1 - (chi(i) - chi(i-1))*(d*e0*Et/(4*k*T))*(Y(6,i)+Y(6,i-1));
s(5,6) = -(chi(i) - chi(i-1))*(d*e0*Et/(4*k*T))*(Y(5,i)+Y(5,i-1));
s(5,15) = s(5,6);

s(6,1) = 0;
s(6,2) = (chi(i) - chi(i-1))*(d*e0*nt/(2*Et*epsilon*epsilon0));
s(6,3:4) = s(6,2);
s(6,5) = -s(6,2);
s(6,6) = -1;
s(6,7:9) = 0;
s(6,10:18) = s(6,1:9);
s(6,15) = 1;
```

```
s(7,1:18) = 0;
s(7,5) = -1/2*(chi(i) - chi(i-1));
s(7,7) = -1;
s(7,14) = s(7,5);
s(7,16) = 1;

s(8,1:18) = 0;
s(8,3) = -1/6*(chi(i) - chi(i-1));
s(8,4) = -1/2*(chi(i) - chi(i-1));
s(8,8) = -1;
s(8,12:13) = s(8,3:4);
s(8,17) = 1;

s(9,1:18) = 0;
s(9,2) = -1/4*(chi(i) - chi(i-1));
s(9,3) = -1/6*(chi(i) - chi(i-1));
s(9,9) = -1;
s(9,11:12) = s(9,2:3);
s(9,18) = 1;

X(:,:,i) = s;

end

%% boundary conditions

% First boundary conditions at x=0
X1(1,1) = 1;
X1(2,6) = 1;
X1(3,7) = 1;
X1(4,8) = 1;
X1(5,9) = 1;

% Second boundary conditions at x=d

XM = zeros(4,9);          % matrix X(M+1)
XM(1,1) = 1;
XM(2,7) = 1;
XM(3,8) = 1;
XM(4,9) = 1;

%% Assemble Coefficient matrix coeff

coeff(1:n1,1:N) = X1;                              % first boudary conditions

for i = 0:M-2
    coeff(n1+i*N+1:n1+(i+1)*N, i*N+1:(i+2)*N) = X(:,:,i+2);
end

coeff(N*M-3:N*M,N*M-8:N*M) = XM;                   % second boudary conditions


%% known right-hand side
```

```
for j = 2:M

E(1,j) = (Y(1,j)-Y(1,j-1)) - (chi(j) - chi(j-1)) * ...
    (d*e0*ke/(2*Jt) * (nt*(Y(2,j)+Y(2,j-1))*((Y(4,j)+Y(4,j-1))/(Y(3,j)+Y(3,j-
1)))^0.5 - nei*nt*(Y(3,j)+Y(3,j-1))*(noi/nri^3)^0.5) - d*e0/Jt*Ge(j));

E(2,j) = (Y(2,j)-Y(2,j-1)) - (chi(j) - chi(j-1)) *...
    (d*Jt/(2*e0*nt*De)*(Y(1,j)+Y(1,j-1))-(d*e0*Et/(4*k*T))*(Y(2,j)+Y(2,j-
1))*(Y(6,j)+Y(6,j-1)));

E(3,j) = (Y(3,j)-Y(3,j-1)) - (chi(j) - chi(j-1)) *...
    (3*d/(2*e0*nt*Dr)*(jg - Jt*(Y(1,j)+Y(1,j-1))/2) -
(d*e0*Et/(4*k*T))*(Y(3,j)+Y(3,j-1))*(Y(6,j)+Y(6,j-1)));

E(4,j) = (Y(4,j)-Y(4,j-1)) - (chi(j) - chi(j-1)) *...
    (-d/(2*e0*nt*Do)*(jg - Jt*(Y(1,j)+Y(1,j-1))/2)-
(d*e0*Et/(4*k*T))*(Y(4,j)+Y(4,j-1))*(Y(6,j)+Y(6,j-1)));

E(5,j) = (Y(5,j)-Y(5,j-1)) - (chi(j) - chi(j-1)) *...
    (d*e0*Et/(4*k*T)) * (Y(5,j)+Y(5,j-1)) * (Y(6,j)+Y(6,j-1));

E(6,j) = (Y(6,j)-Y(6,j-1)) - (chi(j) - chi(j-1)) *...
    (d*e0*nt/(2*Et*epsilon*epsilon0)) * ( (Y(5,j)+Y(5,j-1)) - (Y(2,j)+Y(2,j-
1)) - (Y(3,j)+Y(3,j-1)) - (Y(4,j)+Y(4,j-1)) );

E(7,j) = (Y(7,j)-Y(7,j-1)) - (chi(j) - chi(j-1)) * ( 1/2*(Y(5,j)+Y(5,j-1)) );

E(8,j) = (Y(8,j)-Y(8,j-1)) - (chi(j) - chi(j-1)) * ( 1/2*(Y(4,j)+Y(4,j-1)) +
1/6*(Y(3,j)+Y(3,j-1)) );

E(9,j) = (Y(9,j)-Y(9,j-1)) - (chi(j) - chi(j-1)) * ( 1/4*(Y(2,j)+Y(2,j-1)) +
1/6*(Y(3,j)+Y(3,j-1)) );

end

% At first boundaries

E(n2+1:9,1) = [Y(1,1)-jg/Jt; Y(6,1); Y(7,1); Y(8,1); Y(9,1)];

% At second boundaries

E(1:n2,M+1) = [Y(1,M); Y(7,M)-nci/nt; Y(8,M)-(noi+1/3*nri)/nt; Y(9,M)-
(1/2*nei+1/3*nri)/nt];

% Assemble known right-hand side

B(1:n1) = E(n2+1:9,1);                              % At first boundaries

B(M*N-n2+1:M*N) = E(1:n2,M+1);                      % At second boundaries

for i=0:M-2
    B(n1+1+i*N:n1+(i+1)*N) = E(1:N, 2+i);
```

```
end

B = -B;


%% unkown solution vector, to compare different method

C = [coeff,B];                    % C is augmented matrix, used to scale
for ij = 1:M*N
    C(ij,:) = C(ij,:)/abs(max(C(ij,:)));
end

V = pinv(C(1:M*N,1:M*N))*C(1:M*N,1+M*N);

%% update Y(:,:) matrix by adding incrument V

for ii = 1:M
    Y(:,ii) = Y(:,ii) + V(1+(ii-1)*N:ii*N);
end



%% count the iteration and display the difference

count = count + 1;
disp([count, norm(V)]);
end


Volt = 0.93 + k*T/e0*log(nt*Y(2,1)/NCB);
disp(Volt);
```

B.3. Electron Generation Function

```
%%%%  Electron Generation function
function[Ge] = Gen(chi,d)

load MEC;                % Molar Extinction Coefficient, unit m^2/mol
load phi;                % Irradiation power, unit W/m^2/m

%%%%   Parameter
eta = 0.89;
phi = phi*eta;                      % eta = 1 full sun
h = 6.626 * 10^-34;                 % Boltzman constant
c = 299792458;                      % speed of light, unit m/s
PE = h * c ./ (MEC(:,1)*10^-9);     % Photon energy, uint J
IPE = phi(:,2)./PE;                 % Incident Photon flux, unit /m^3/s


Rf = 1000;        % roughness factor (function of porosity and particle size)
```

```
sigma = 1.3*10^-6;   % concentration of dye adsorbed on an ideal(virtual)flat
surface unit: mol/m^2
cdye = sigma * Rf / (10*10^-6);         % concentration of the dye in the
cell, mol/m^3
alpha = MEC(:,2) * cdye / log(exp(1));  % absorption coefficient of the dye,
unit m^-1

x = size(chi);
M = x(2);
Ge = zeros(M,1);

for i = 1:M
    psi = alpha.*IPE.*exp(-alpha*chi(i)*d);    % unit /m^2/s
    t = MEC(:,1); t = t*10^-9;                 % unit convert from nm to m
    Ge(i) = trapz(t,psi);                      % unit /m/s
end
```

LIST OF PUBLICATIONS

1. J. Gong, J. Liang, and K. Sumathy. "Review on dye-sensitized solar cells (DSCs): Fundamental concepts and novel materials," *Renewable & Sustainable Energy Reviews*, 16(8): 5848-5860, 2012.

2. J. Gong and K. Sumathy. "A theoretical study on third generation photovoltaic technology: dye-sensitized solar cells," *Proc. Of Int. Conference on Renewable Energies and Power Quality* (ICREPQ'12), Santiago de Compostela, Spain, March 28-30, 2012. (Orally presented).

3. J. Gong, K. Sumathy, and J. Liang. "A Simplified Electrical Model of the Dye-Sensitized Photoelectrochemical Cell," *International Journal of Sustainable Energy*, 2013 (In press)